Journal of Marine Science and Technology

Volume 26 | Issue 3 Article 3

STUDY ON PROBABILISTIC MEAN FEATURES OF LOWER AND UPPER FREE-SURFACE PROFILES AND VELOCITY FIELDS OF A HIGHLY FLUCTUATING FREE JET OVER A CHUTE

Chang Lin
Department of Civil Engineering, National Chung Hsing University, Taiwan, R.O.C, chenglin@nchu.edu.tw

Ming-Jer Kao
Department of Civil Engineering, National Chung Hsing University, Taiwan, R.O.C

James Yang
Royal Institute of Technology (KTH), Stockholm, Sweden

Peng-Hua Teng
Division of Resources, Energy and Infrastructure, Royal Institute of Technology (KTH), Stockholm, Sweden.

Rajkumar Venkatesh Raikar
Department of Civil Engineering, KLE Dr. M. S. Sheshgiri College of Engineering and Technology, Udyambag, Belagavi, Karnataka, India.

Recommended Citation

Lin, Chang; Kao, Ming-Jer; Yang, James; Teng, Peng-Hua; and Raikar, Rajkumar Venkatesh (2018) "STUDY ON PROBABILISTIC MEAN FEATURES OF LOWER AND UPPER FREE-SURFACE PROFILES AND VELOCITY FIELDS OF A HIGHLY FLUCTUATING FREE JET OVER A CHUTE," *Journal of Marine Science and Technology*: Vol. 26: Iss. 3, Article 3.
DOI: DOI: 10.6119/JMST.201806_26(3).0003
Available at: https://jmstt.ntou.edu.tw/journal/vol26/iss3/3

STUDY ON PROBABILISTIC MEAN FEATURES OF LOWER AND UPPER FREE-SURFACE PROFILES AND VELOCITY FIELDS OF A HIGHLY FLUCTUATING FREE JET OVER A CHUTE

Acknowledgements

The study presented here was carried out as part of a Ph. D. project “Hydraulic design of chute spillway aerators”, funded by Swedish Hydropower Centre (SVC). SVC has been established by the Swedish Energy Agency (Energimyndigheten), Energiforsk AB and Svenska Kraftnät together with Royal Institute of Technology (KTH), Luleå University of Technology (LTU), Chalmers University of Technology (CHT) and Uppsala University (UU), with the website of www.svc.nu. The authors are indebted to Ms. Sara Sandberg of SVC and Ms. Maria Bartsch of Svenska Kraftnät for project co-ordinations

Journal of Marine Science and Technology, Vol. 26, No. 3, pp. 309-326 (2018)
DOI: 10.6119/JMST.2018.06_(3).0003

STUDY ON PROBABILISTIC MEAN FEATURES OF LOWER AND UPPER FREE-SURFACE PROFILES AND VELOCITY FIELDS OF A HIGHLY FLUCTUATING FREE JET OVER A CHUTE

Chang Lin[1], Ming-Jer Kao[2], James Yang[3],
Peng-Hua Teng[4], and Rajkumar Venkatesh Raikar[5]

Key words: free jet, air-water interface, high-speed particle image velocimetry (HSPIV), gray-level gradient, contrast-enhancement techniques, probabilistic mean.

ABSTRACT

An optic-based method that utilizes the particle-laden images captured during high-speed particle image velocimetry (HSPIV) measurements is presented, aiming to explore the *probabilistic mean characteristics* of the free surface profiles and velocity fields of a free jet with high-frequency random fluctuations over a chute. The technique based on the gray-level gradients in the smoothed gray level distribution of the contrast-enhanced images is used to determine the probabilistic mean features of the free jet, right beneath and above which the water-air interfaces have I%/(100 − I)% intermittent appearance of air/water phase and (100 − I)%/I% fitful show-up of water/air phase. Further, the cross-correlation calculation for HSPIV measurements is employed to obtain the instantaneous and probabilistic mean velocity fields of the free jet. A target experiment of the free jet having a mean water-depth of 2.76 cm and a Froude number of 3.92 over a 17° chute model is performed in a re-circulating water channel to demonstrate the application of this method.

The entire process for obtaining the probabilistic mean positions of the free surface profiles is elucidated step-by step. The lower/upper part of the free surface changing from the height at which the possibility of intermittent appearance of water phase is 3%/97%, via the counterpart for 50%/50%, to that for 97%/3% is identified precisely. In addition, the probabilistic mean velocity field is further categorized into the conditionally and overall time-averaged ones. Each streamwise velocity profile in the conditionally time-averaged velocity field is fairly uniform. However, the counterpart in the overall time-averaged velocity field evidently shows the non-uniform feature with prominent velocity gradient in the lower/upper part between the height at which the possibility of intermittent appearance of water phase is 3%/97% and the counterpart is 97%/3%.

I. INTRODUCTION

Free jet characterized by the nappe-shaped supercritical stream with the lower and upper free surfaces can be seen frequently in hydraulic engineering such as flow over a vertical drop with/without end-sill built across a man-made channel or a weir constructed across a river (Lin et al., 2007; 2008a, b), flow over a chute with an offset and/or a deflector (Liu, 2007), and flow downstream of a spillway having a flip bucket (Vischer and Hager, 1995). Free jets can be also formed by localized erosion of channel bed due to evolution in the upstream migration of headcuts, which have sudden step-like changes in bed elevation (Bennett and Alonso, 2006).

The *free jet over a vertical drop* is generally a *subcritical* approaching stream that runs over a 90° sharp-edged vertical drop and leaves the brink as a supercritical nappe-shaped jet, and then becomes a sliding jet soon after touching upon and ridding over the recirculating water cushion. On the other hand, the *free jet over a chute* is a high-speed *supercritical* stream, which occurs downstream of an offset and/or a deflector deployed

submitted 12/18/17; revised 02/27/18; accepted 03/21/18. *Author for correspondence: Chang Lin (e-mail: chenglin@nchu.edu.tw).*
[1] *Department of Civil Engineering, National Chung Hsing University, Taiwan, R.O.C.*
[2] *Department of Civil Engineering, National Chung Hsing University, Taiwan, R.O.C.*
[3] *Royal Institute of Technology (KTH), Stockholm, Sweden.*
[4] *Division of Resources, Energy and Infrastructure, Royal Institute of Technology (KTH), Stockholm, Sweden.*
[5] *Department of Civil Engineering, KLE Dr. M. S. Sheshgiri College of Engineering and Technology, Udyambag, Belagavi, Karnataka, India.*

across a chute and has the napped jet with prominent irregular fluctuations in its lower and upper free surfaces. Therefore, understanding the features of free jet and associated evolution becomes very important for accessing the impact force on the chute surface, for designing a downstream pool for energy dissipation, and for predicting the upstream migration of headcut erosion.

A pioneering study on the characteristics of free jets with subcritical approaching flows toward the brink and supercritical flows projecting from the brink of a vertical drop was carried out experimentally by Moore (1943), revealing that energy loss is highly associated with the relative depth of the approaching flow (= the ratio of the critical depth of approaching flow to the height of vertical drop). Using a dimensionless parameter known as the drop number, Rand (1955) developed empirical equations to illustrate the feature of free jet downstream of a vertical drop. Further, Marchi (1993) proposed an analytic model to predict the lower and upper free surfaces of a free jet over a vertical drop. A comparison of both the lower and upper free surfaces of the free jet between experimental data and those predicted using Marchi (1993)'s analytic model was made by Lin et al. (2007) for the case of a subcritical approaching flow (running over a horizontal base upstream of the vertical drop). Rajaratnam and Chamani (1995) reported the measurement results of velocity profiles in the jets over a vertical drop using Prandtl probes. However, inevitable flow-induced vibration of the probes (with external diameters of 2.6 and 3.2 mm) being intruded into the high-speed jet flow can lead to the flow interference and incur potential measuring error. Further, Lin et al. (2007) utilized fiber laser Doppler velocimeter (FLDV) to explore the feature of mean velocity profiles in the jets over the vertical drops under the condition of subcritical approaching flow with full ventilation.

On the other hand, supercritical free jet over a chute resulted from an offset or a deflector can entrain air into water flow mainly from the wedged tip of the air cavity located downstream of the free jet. Most previous researches on chute flow paid attention to the characteristics of air concentration distribution during the entrainment or detrainment process far downstream of the wedged tip of air cavity; and to the effects of various parameters, including the slope of chute, the heights of offset and deflector, and the relative sub-pressure exerted in the air cavity (e.g., Rutschmann and Hager (1990); Gaskin et al. (2003); Kramer et al. (2006); Pfister and Hager (2011)). On the contrary, associated investigations on the features of free surface profiles and velocity fields of the high-speed free jet over a chute are still very rare. As reported by Bennett and Alonso (2006) and Yang et al. (2014), the high-speed free jet with very prominent irregular fluctuation and highly unsteady feature makes various kinds of measurements fairly difficult.

Recent advancement and application of non-invasive measuring techniques, such as PIV and HSPIV for velocity measurements and ultrasonic gauge for free surface detection in such a high-speed flow, can help in avoiding flow interference and severe splash or upwelling of the free surface due to intruding measuring probes into the high-speed free jet, thus significantly enhancing the measurement precision and experimental quality. Nevertheless, the point-by-point measurement of the (upper) free surface of the free jet using ultrasonic gauge is fairly time consuming and sometimes does not work well due to the interference effect caused by severe splash of many air droplets over the free surface on the appropriateness of the output signal of ultrasonic sensor. Moreover, the measurement of the lower free surface of the free jet employing ultrasonic gauge becomes totally impossible due to existence of the air cavity underneath the free jet. Such measurement problems highly motivates towards developing a measurement technique for exploring not only the lower and upper free surface profiles but also the velocity fields of the free jet over a chute. Therefore, the present study emphasizes on the application of HSPIV measurements for exploring the *probabilistic mean features* for the lower and upper free-surface profiles and velocity fields of high-speed free jet with prominent random fluctuation, which takes place between the brink of the offset and the section upstream of the wedged tip of air cavity over the chute surface.

II. EXPERIMENTAL SET-UP AND EXPERIMENTATION

1. Water Channel, Chute Model and Coordinate System

The recirculating water channel with a test section having dimension of 3.05 m long, 0.50 m wide and 0.54 m deep located at the Hydraulics Laboratory of the Department of Civil Engineering, National Chung Hsing University, Taiwan was used for experimentation. The test section located at 3.0 m from the inlet of the channel is provided with two glass-sided walls and glass bottom to facilitate optical access. The flow recirculation in the channel is facilitated through a control unit having a feedback circuit and a butterfly valve.

The chute model is made of acrylic plate and mounted from the start of the test section with related deployment being illustrated in Figs. 1(a) and (b). The chute model has dimension of a horizontal length of 135.0 cm, a spanwise total-width of 49.5 cm, and a maximum vertical height of 41.0 cm; together with a total chute-length of 124.0 cm and an offset having a height of $H = 3.2$ cm. The inclination of the entire stepped-chute part is 17° with reference to the horizontal bottom of the water channel. A rectangular-shaped honeycomb, consisting of a bundle of straws, is installed upstream of the inlet of chute flow and used to smooth the oncoming flow. No deflector is installed in the present study, aiming to simplify the chute geometries and exclude the effects of the deflector dimensions (including the slope, length and height of the deflector) on the feature of the free surface profiles of free jet. Natural ventilation through a slot on a vertical plate, mounted flush over the chute model and parallel to the side-wall glass with a clear spacing of 6.25 cm in between, can provide sufficient air supply to the chute flow (see Figs. 1(a) and (b). An air cavity is thus formed downstream of the offset and beneath the free jet.

A Cartesian coordinate system (X, Y) is used with X being measured positive towards downstream and Y positive upwards

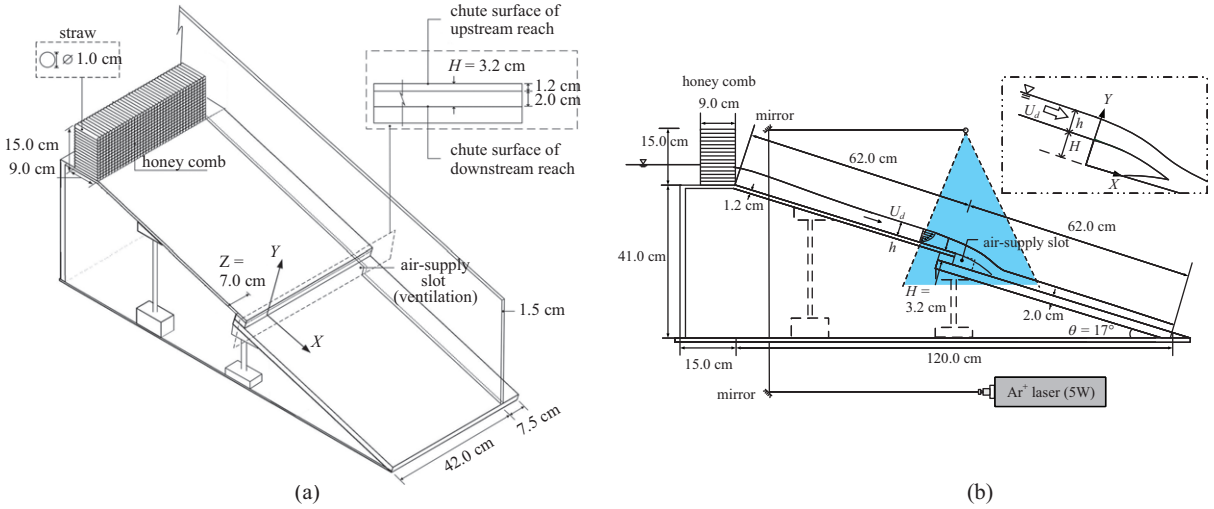

Fig. 1. Diagram showing detailed dimensions of chute model and coordinate system: (a) 3-D view; (b) side view along with deployment of laser light sheet.

from the offset bottom, as illustrated in Figs. 1(a) and (b). The origin is located at the brink of the offset bottom and 7.0 cm away from the nearer side-walled glass to acquire the optimal observation of random oscillations on the lower and upper free surfaces of the free jet but without the side-wall boundary effect. The time-averaged streamwise and transverse velocity components in the X and Y directions are herein defined as $U(X, Y)$ and $V(X, Y)$, respectively.

Only one experiment is performed to realize the objectives of this study. The approaching flow has a mean water depth h = 2.76 cm, a depth-averaged velocity U_d = 203.84 cm/s, a unit discharge q = 562.6 cm^2/s, and a Froude number of F_r (= U_d/(gh)$^{1/2}$) = 3.92 measured at X = -4.0 cm, evidently revealing the flow is *supercritical*.

2. Measurements of Instantaneous Free Surface Elevations Using Ultrasonic Sensor

To witness very random oscillations on the upper free surface of the free jet with high-frequency fluctuations, point measurements of the free surface elevations are conducted using an ultrasonic sensor (Banner U-GAGE S18U). The sensor has a full output range varying from 0 to 10 voltages for detecting the (instantaneous) distance between the targeted free surface of the jet and the sensor surface from 3.0 cm to 30.0 cm with a response time and frequency of 2.5 ms and 400 Hz, respectively. During the calibration process, the ultrasonic sensor was mounted upon a steel frame structure which was attached to a three-dimensional translation table. The movement of the table can be precisely controlled by three optical meters and three digital monitors (with a precision of 0.01 mm). By moving the translation table (together with the sensor) vertically up and down with respect to the still water level, each run which has vertical displacements ranged from 0 cm to 3.0 cm with an increment of 0.25 cm was tested. The output response of each run for a given displacement is found to be almost the same as the other run, as shown in Fig. 2. Taking the tests with two displacements of 1.5 cm and

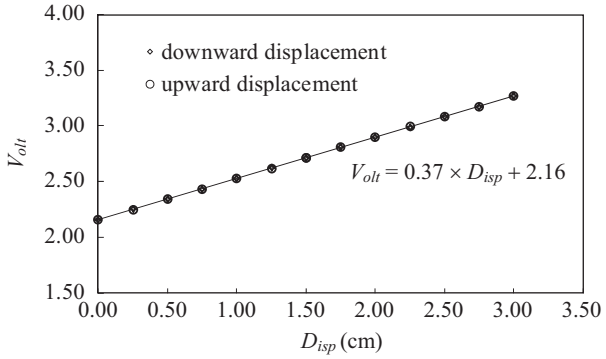

Fig. 2 Relationship between output voltage response, V_{olt}, and relative displacement with respect to still water level, D_{isp}, for measurement of upper free surface elevations using ultrasonic sensor.

3.0 cm for example, the respective relative measuring errors are found to be only 0.15 % and 0.16 %, demonstrating high repeatability of the sensor outputs and very tiny errors in measuring the free surface elevations. It is also seen that the output response of the sensor is demonstrated to be 0.370 V_{olt}/cm with a R^2 value of 0.999, indicating very good linearity between the output voltage and the input free surface elevation.

3. HSPIV Measurements for Velocity Fields

The purposes of utilizing HSPIV system is of twofold. One is to measure the (two-dimensional) instantaneous and probabilistic mean velocity fields of *water stream* in the approaching flow/free jet on the upstream/downstream side of the offset. The other is to determine the instantaneous and probabilistic mean features for the free surface profiles of the free jet.

The HSPIV system is composed of a high-speed digital camera, laser head along with laser light sheet, and the seeding particles dispersed in the water flow. Aluminum particles with a mean diameter of 30.6 μm and a specific gravity of 2.7 were used as the seeding particles, which were uniformly dispersed

in the water mass in the recirculating water channel. The settling velocity of aluminum particles (according to Stoke's law) is less than 0.09 cm/s, which is much smaller than the velocity of interest in this study. The light source used is a 5 W argon-ion laser. The laser beam was emitted from the laser head being placed under the glass bottom of the water flume, then reflected by a series of mirrors before passing through a cylindrical lens with a diameter of 0.57 cm, thus forming a light sheet (with a thickness of 1.5 mm) projecting downward into the flow (see Fig. 1(b)).

A high-speed digital camera (Vision Research, Phantom M310) with a maximum pixel resolution of 1,280 × 800 under a maximum framing rate of 3,200 Hz, was used to capture the particle-laden images. To allow high image resolution and appropriate magnification of the measuring area, a Nikon 105 mm lens (f/2.8D AF Micro-Nikkor) was fitted to the camera. The images of flow fields characterized by the movement of seeding particles were continuously recorded using the camera. To ensure a high time-resolved HSPIV algorithm, a framing rate of 4,000 Hz with a resolution of 1024 × 800 pixel was particularly set while capturing the images of velocity fields. The captured images were then processed using cross-correlation technique to obtain the instantaneous velocity field of water flow. A multi-grid interrogation process starting at 64 × 64 pixels and ending at 8 × 8 pixels with 50% overlap were used in processing the data.

It is important to mention that the camera was mounted on an angle vice, which not only features accurate adjustments on setting obliqueness but also provides an extra degree of freedom in rotation (continuous 90° from horizontal to vertical). Under such a situation, the upper and lower edges in each field of view (FOV) of the camera were precisely adjusted parallel to the surface of the stepped-chute part. In order to obtain detailed velocity fields of water stream in the approaching flow/free jet upstream/downstream of the offset with better spatial resolution, a total of three fields of view (FOV_1 to FOV_3) for HSPIV measurements are considered. The deployment of FOVs is shown in Fig. 3, together with indication of not only the regions of approaching flow, free jet and air cavity; but also the positions of the (instantaneous) upper and lower free surfaces and the wedged tip of air cavity. The size of FOV_i (i = 1 ~ 3) in the HSPIV measurement is 5.22 cm × 4.08 cm. All of the FOV_i for HSPIV measurements cover the streamwise distance from X = -4.5 cm to X = 9.0 cm approximately. The adjacent fields of view for HSPIV measurements have certain overlaps to ensure continuous construction of the global velocity field by using the mosaic technology. Six runs were repeated for each field of view with per run having 9,000 continuous measurements.

A process for intensifying the image contrast was performed by using the Laplacian edge-enhancement technique (Adrain and Westerweel, 2011) and Image Processing Toolbox function *imadjust* (Gonzalez and Woods, 2008; Gonzalez et al., 2009). The images obtained were deduced from the background images in order to exclude any constant noise source. Therefore, the mean velocity field for the entire free jet is a mosaic of HSPIV measurements from the FOV_2 and FOV_3.

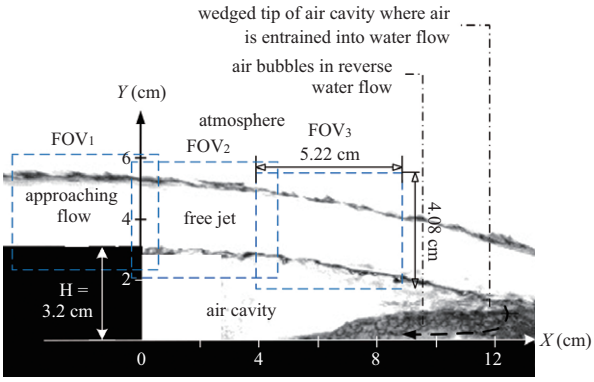

Fig. 3. Diagram for deployment of FOVs for HSPIV measurements.

4. HSPIV Measurements for Probabilistic Mean (Lower and Upper) Free-Surface Profiles

The second objective of using the HSPIV system is to determine the instantaneous and probabilistic mean free-surface profiles of the free jet. While recording the images captured by the high-speed camera, the water stream was seeded with aluminium particles being distributed uniformly in the flow and illuminated by the laser light sheet. Thus, many brightened speckles or pathlines recorded in each image represent the footprints of the seeded particles existing in the water stream of free jet. Further, two relatively dark areas with one being located beneath the free jet (i.e., the air cavity) and the other right over the free jet (i.e., the atmosphere) are also observable in each image. Under such a condition, two water-air interfaces exist in the image between the lower darkened air cavity and the brightened free jet as well as between the brightened free jet and the upper darkened atmosphere. Accordingly, a series of the recorded images are then presented in terms of grey level representation, i.e., the instantaneous grey level distributions. An ensemble-averaging for several thousands of these particle-laden images is next conducted to obtain the ensemble-averaged grey level distribution. A symmetric (2n+1) smoothing scheme is further used to smooth the ensemble-averaged grey level distribution, aiming to obtain the plot of smoothed grey level distribution. Based on some criteria (to be identified and stated later), the probabilistic mean upper and lower free-surface profiles of the free jet can thus be determined from the smoothed grey level distribution.

III. RESULTS AND DISCUSSIONS

1. Characteristics of Approaching Flow Upstream of Offset

The instantaneous velocity field of the supercritical approaching flow was first measured by HSPIV in FOV_1 for -4.5 cm ≤ X ≤ 0.5 cm. The mean velocity field and free surface profile of the approaching flow are shown in Fig. 4, exhibiting that the mean velocity field has the feature of accelerated flow with U_d = 203.84 cm/s and F_r = 3.92 at X = -4.0 cm as well as U_d = 214.73 cm/s and F_r = 4.24 at X = 0 cm (i.e., the brink of the offset). Further, the decrease of the mean water depth from h =

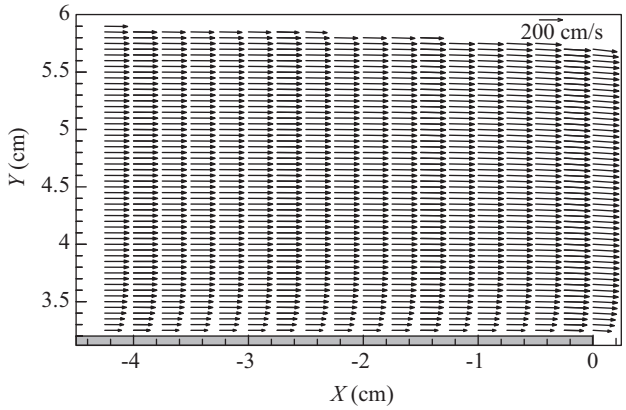

Fig. 4. Mean velocity field and free surface profile of approaching flow for -4.5 cm ≤ X ≤ 0 cm.

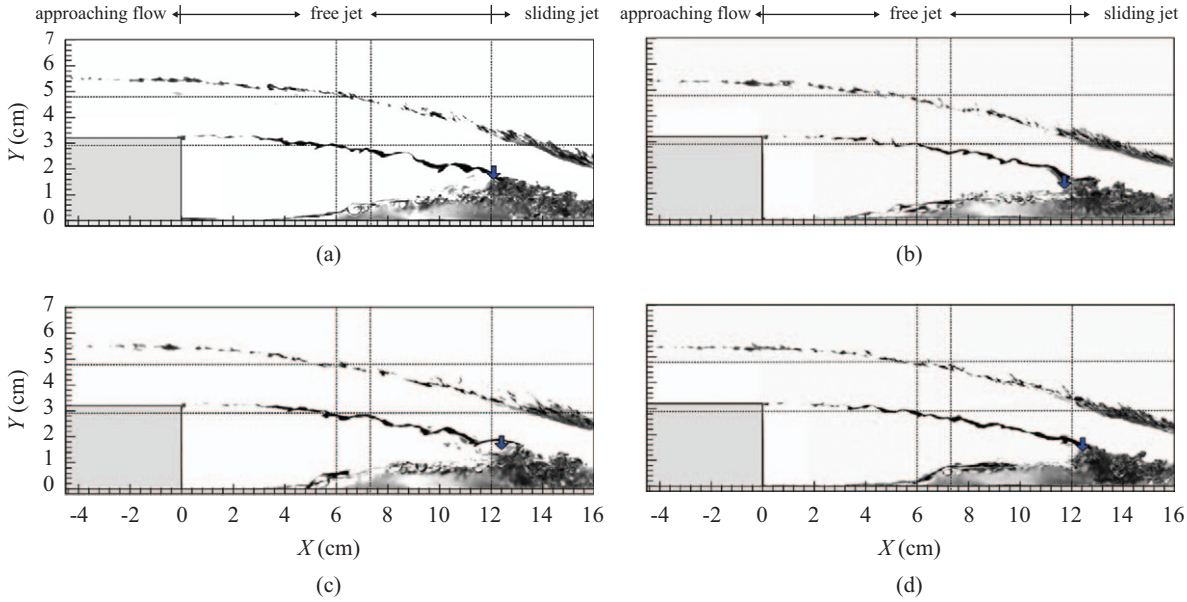

Fig. 5. Four instantaneous flow images of free jet with upper and lower free surfaces fluctuating randomly, together with irregular drifting of wedged tip of air cavity.

2.76 cm at X = -4.0 cm to h = 2.62 cm at X = 0 cm (i.e., the brink section of the offset) is evidenced clearly. The offset acts like a drop structure such that the transformation of the approaching flow into the projecting free jet commences near the brink of the drop structure, around which the depression of the free surface takes place (Lin et al., 2007). Meanwhile, the mean unit discharge q_m is estimated to be 562.6 cm^2/s for -4.0 cm ≤ X ≤ 0 cm. The maximum relative error of the unit discharge with respect to the mean value is only 0.14%, highlighting very good consistency and high precision in the velocity and water depth measurements of the approaching flow.

Following the method used by Lin et al. (2012a), assuming the flow to be two-dimensional, a continuity check was carried out to calculate the flux of each grid element $f = |\partial U/\partial X + \partial V/\partial Y| \cdot dA$ (in which $\Delta X = \Delta Y$ = 0.41 mm of each grid element is used and dA is the area of a grid element) in the velocity field. The relative error of the flux of the velocity field is defined as f/f_0 (where $f_0 = U_d \times \Delta Y$). The typical error in the values of this velocity field at most locations with relatively low velocity gradient is less than 1.8%, and the counterpart at locations having prominent velocity gradient region near the chute surface is 3.9%, demonstrating fairly precise measurements in the velocity field of the approaching flow.

2. High-frequency Random Fluctuations of Free Surface Elevations of Free Jet

A global view for the instantaneous flow field of free jet is illustrated at first for visual aid and easy comprehension. The free jet having both the lower and upper free surfaces is illustrated in Figs. 5(a)-(d). The sliding jet being transformed from the free jet and riding on the water-air bubble interface is located downstream of the mean position for the wedged tip of air

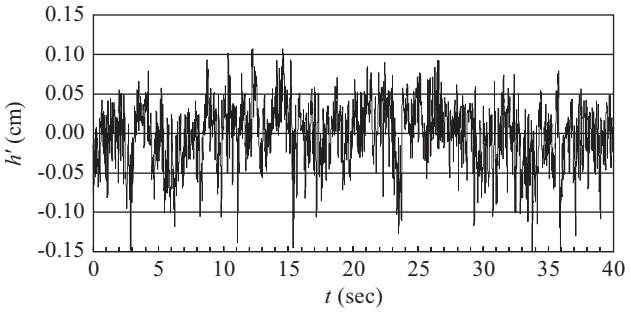

Fig. 6. Time series of random fluctuations in upper free surface elevation of free jet measured at X = 7.27 cm.

cavity (at X = 12.0 cm, as shown by the arrow in each subfigure), beneath which air bubbles move in reverse water flow over the chute surface. However, the feature of air bubbles being entrained into the sliding jet and the reverse water flow will not be studied in the present study due to the main focus on the characteristics of free jet.

For clear visualization of the temporal and spatial variations of the upper and lower free surface elevations as well as the position of the wedged tip of air cavity, two parallel lines with Y = 2.90 cm and Y = 4.80 cm are marked in Figs. 5(a)-(d). In addition, the other three parallel lines with X = 6.00 cm, X = 7.27 cm and X = 12.00 cm all perpendicular to the former two lines are also plotted. It is easily found that the upper and lower free-surface elevations moves up and down randomly with reference to the four intersection points, say (X, Y) = (6.00, 4.80) cm and (6.00, 2.90) cm as well as (7.27, 4.80) cm and (7.27, 2.90) cm, clearly demonstrating irregular fluctuation of the free surfaces of the free jet. As also observed from Figs. 5(a)-(d), variation of the instantaneous position for the wedged tip of air cavity is witnessed obviously with respect to its mean position located at (12.00, 1.64) cm. This evidence strongly demonstrates that the position for the wedged tip of air cavity not only drifts upstream and downstream randomly, but also oscillates up and down irregularly with respect to its mean position.

Fig. 6 presents one of the examples for the time series of random fluctuations (with respect to the zero mean) in the upper free-surface elevation of the free jet, $h'(t)$, which was measured at X = 7.27 cm using ultrasonic sensor for time t being varied from 0 s to 40.0 s. Many random fluctuations h' (t) oscillating between -0.15 cm and 0.11 cm can be evidenced in the time series. The maximum extent of the random fluctuations in the Y direction can be regarded as 0.26 cm approximately, which is about 1/10 of the mean water depth at the brink section (i.e., h = 2.62 cm at X = 0 cm). Note that exhibition of the counterpart for the lower free-surface elevation becomes impossible due to use of the ultrasonic sensor, but can be still witnessed from the images captured by the high-speed camera.

3. Original and Firstly Contrast-Enhanced Images

Fig. 7(a) illustrates one of the original images of the free jet for 3.95 cm ≤ X ≤ 9.15 cm. Many pathlines with different

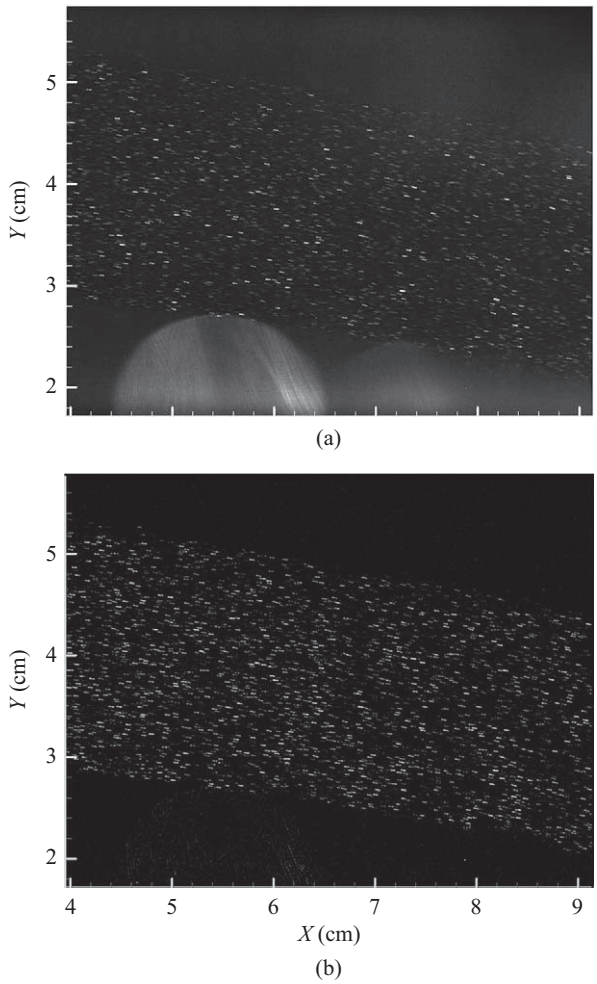

Fig. 7. One of images showing pathlined flow field of free jet for 3.95 cm ≤ X ≤ 9.15 cm, (a) original image; (b) post-CE_1 image.

brightened segments, which highlight the "footprints" of the seeding particles, can be seen in the free jet. Furthermore, two half-circle-like white spots, induced by scattering of the laser light sheet and then reflected by the air-bubble surfaces, are situated on the lower part of Fig. 7(a). With reference to Fig. 7(a), the firstly contrast-enhanced (hereafter named "CE_1") image is presented in Fig. 7(b) using the Laplacian edge-enhancement technique (Adrain and Westerweel, 2011). It is seen that the total number of highly brightened pathlines (or particle traces) has been evidently increased as compared with that shown in Fig. 7(a), and that the corresponding bright areas of the two white spots with constant background brightness have been totally removed. The positions for the instantaneous lower and upper free surfaces of the free jet can be easily identified, for example, to be Y = 2.44 cm and Y = 4.80 cm, respectively, at X = 7.27 cm.

4. Instantaneous and Ensemble-averaged Gray Level Distributions

Fig. 8 illustrates the ***instantaneous gray level distributions*** along a specified line located at X = 7.27 cm for 1.70 cm ≤ Y ≤

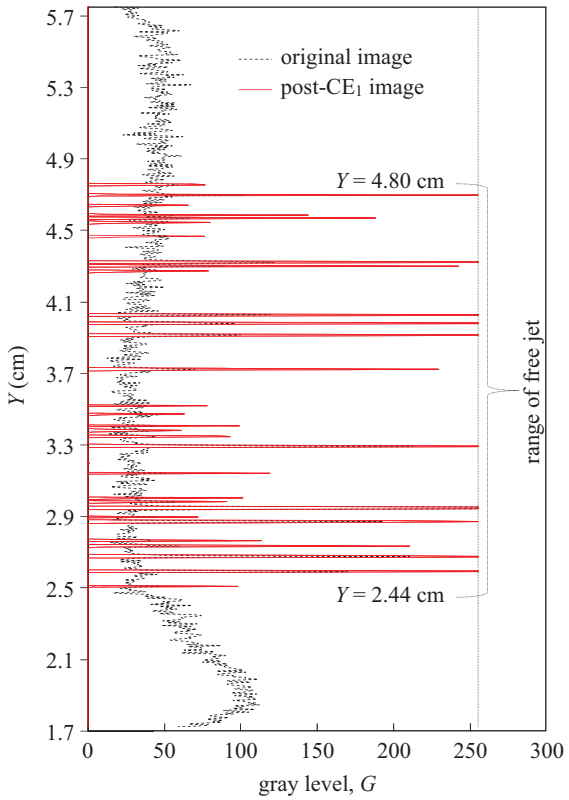

Fig. 8. Instantaneous gray level distributions with black and red plotting obtained at $X = 7.27$ cm for original and post-CE_1 images, respectively.

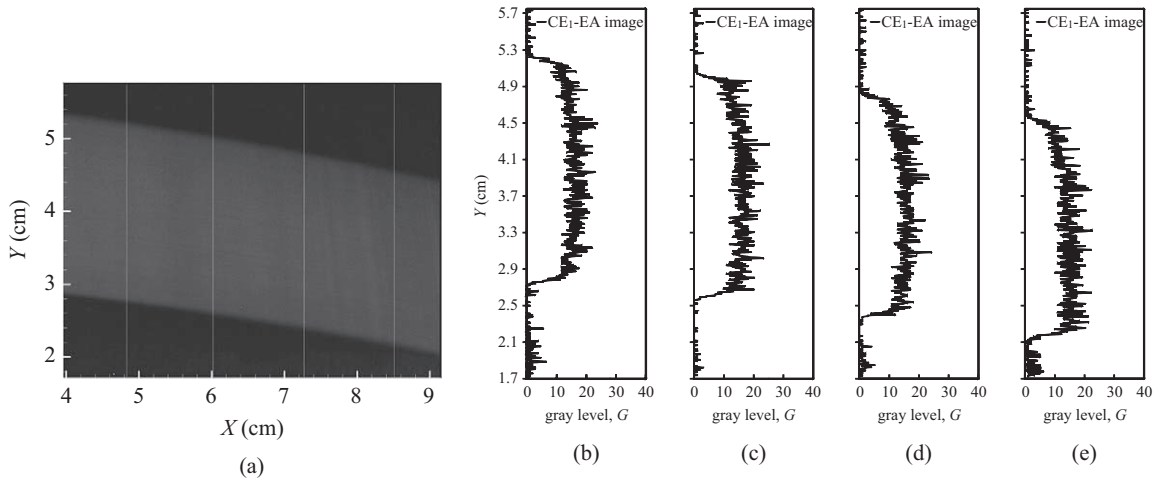

Fig. 9. (a) CE_1-EA image with a total of 4000 frames; (b ~ e) CE_1-EA gray level distributions at $X = 4.83$ cm, 6.02 cm, 7.27 cm and 8.51 cm, respectively.

5.75 cm for the original and CE_1 images shown in Figs. 7(a) and (b). Note that the mean size of the seeding particle (= 30.6 μm) is equal to 0.6 pixels and the conversion factor between centimeter and pixels shown in Fig. 8 is 0.0051 cm/pixel or 196.08 pixel/cm. Relatively low gray level distribution in the original image is witnessed, except for those spike-like peaks with gray levels over 65 up to 210. On the other hand, very pronounced brightness enhancement for the seeding particles in the CE_1 image leads to significant increase of gray level ranging from 65 up to the maximum value of 255. Note that the large half-circle spot, through which the line $X = 7.27$ cm passes in the original image, contributes a prominent hump of the gray level. This hump-shaped gray level starts from 110 at $Y = 1.85$ cm and keeps increasing up to a peak of about 115 around $Y = 1.8$ cm, and then decreases to a value of about 21 at $Y = 2.4$ cm. However, the hump-shaped gray levels have been substantially reduced to nearly zero in the CE_1 image. Accordingly, the gray levels for most seeding particles existing between the instan

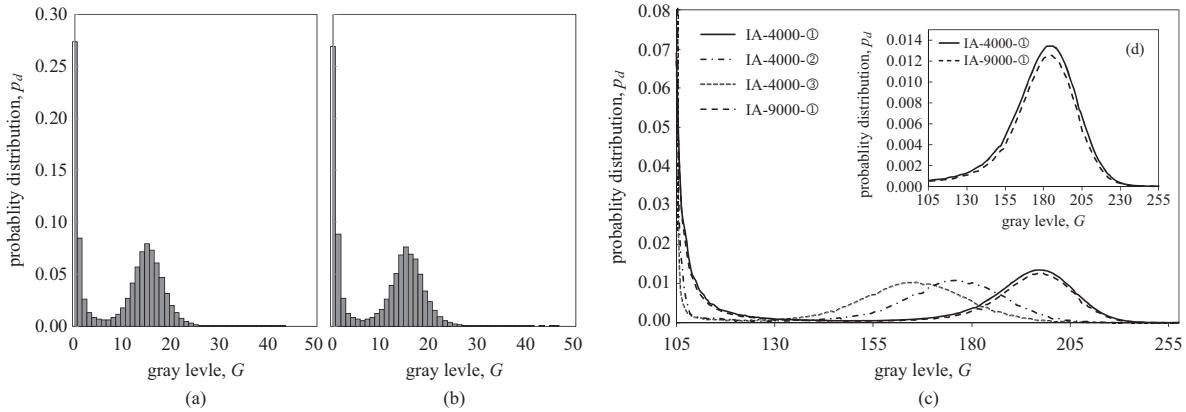

Fig. 10. Probability histogram of gray level (a) post-CE_1 with 4000 frames; (b) post-CE_1 with 9000 frames; (c) after IA manipulations with different G_{Pi} (i = 1 ~ 4); (d) magnified view of histograms with IA-4000-① and IA-9000-① manipulations.

taneous lower and upper free surfaces (situated between Y = 2.44 cm and Y = 4.80 cm) for X = 7.27 cm are greatly enhanced up to a value ranging from 65 to 255. Following the similar procedure mentioned above, a "time series" of the instantaneous gray level distributions for the CE_1 images for X = 7.27 cm or elsewhere can be thus obtained.

Further, the ensemble-averaged images can be obtained subsequently by using a series of CE_1 images with a total of frames varying from 1000 to 9000 (with per increase of 1000 frames). Fig. 9(a) presents such a post-CE_1 ensemble-averaged (hereafter called as "CE_1-EA") image with a total of 4000 frames for 1.70 cm ≤ Y ≤ 5.75 cm. It is also found that the CE_1-EA counterparts of free jet for using N (= 5000 ~ 9000) frames are slightly darker than that of 4000-frame image if N gets larger (not shown). Figs. 9(b)-(e) show four ***CE_1-EA gray level distributions*** along the lines located at X = 4.51 cm, 6.02 cm, 7.27 cm and 8.51 cm, respectively. In each of the profile, a trapezoid-shaped gray level distribution is clearly seen, exhibiting a nearly constant top-hat around which many spikes exist in the central part and below/beyond which a gradient-like subzone appears around the lower/upper free surface. The relatively larger gray levels of the central part identify the response of *water phase* from the free jet for different positions. On the other hand, the dark area with relatively low gray levels, which represent the response of *air phase* from the air cavity/atmosphere, is located outside of the lower/upper free surface. The averaged values of these top-hats shown in Figs. 9(b)-(e) are 15.03, 15.47, 14.65 and 15.42, respectively. It should be mentioned that there is a corresponding top-hatted gray level along any one of the 1024 lines (with each line being located at a "pixel position" varying from 1 to 1024 in the X direction). An average of these 1024 top-hats is calculated to be 15.20, representing the *global mean* gray level of the free jet (based on the use of seeding particles), however, which is much smaller as compared with the maximum counterpart of 255.

5. Secondary Contrast-enhanced Images and Smoothed Gray Level Distribution

To enhance the CE_1-EA images with more pronounced contrast for the water phase, an enlargement of the difference between the *global mean* of these constant top-hats in the central part and the relatively low gray levels appearing outside of the lower and upper surfaces becomes necessary. The function ***imadjust*** (IA) with histogram specification, which is one of the fundamental Image Processing Toolbox functions for *gray-level transformation of gray-scaled images* (Gonzalez and Woods, 2008; Gonzalez et al., 2009), is employed to realize the secondary contrast enhancement of the free jet in the CE_1-EA images. Details of the principle and manipulation of IA and histogram specification can be referred to Gonzalez et al. (2009) (in pages 80-83 and 101-107). Direct use of IA manipulations with distinct histogram specifications is illustrated in the following.

In the present study, a total of 1024 × 800 (= 819,200) pixels exist in the image with each pixel position having a corresponding gray level. By calculating the occurrence times for all of the gray levels (varying from 0 to 255) throughout the 819,200 pixel positions in the CE_1-EA image, a histogram exhibiting the relationship between either the occurrence times (i.e., frequency) or the probability and the gray level can be constructed accordingly. Figs. 10(a) and (b) present the histograms of the CE_1-EA images for 4000-frame and 9000-frame cases, respectively. In Fig. 10(a), the two largest probabilities (= 0.2737 and 0.0846) takes place in the dark area for the gray levels being equal to zero and unity, respectively, reflecting the *air phase* from either the air cavity or the atmosphere. Further, the third peak probability (= 0.0794) appears at the gray level of 15, which highlights the *water phase* from the free jet and covers the range between 14.5 and 15.5 as evidenced for the top-hatted values labeled in Figs. 9(b)-(e). On the other hand, for 9000-frame case, the two largest probabilities (= 0.2691 and 0.0889) take place for the gray levels being equivalent to zero and unity; and the third peak one (= 0.0758), which is less than that for 4000-frame counterpart, occurs also at the gray level of 15.

By using the function IA with histogram specification mentioned above, four new histograms transformed from those shown

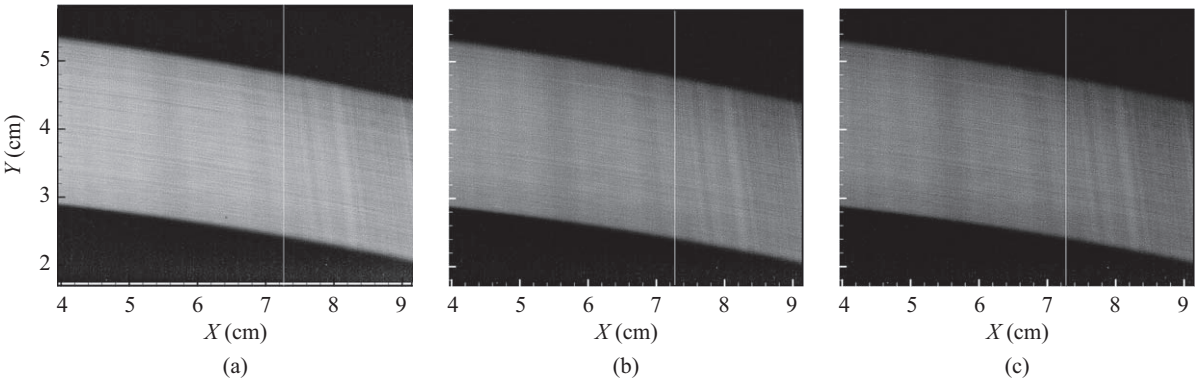

Fig. 11. Post-CE_2 images with (a) IA-4000-①; (b) IA-4000-②; (c) IA-4000-③ manipulations.

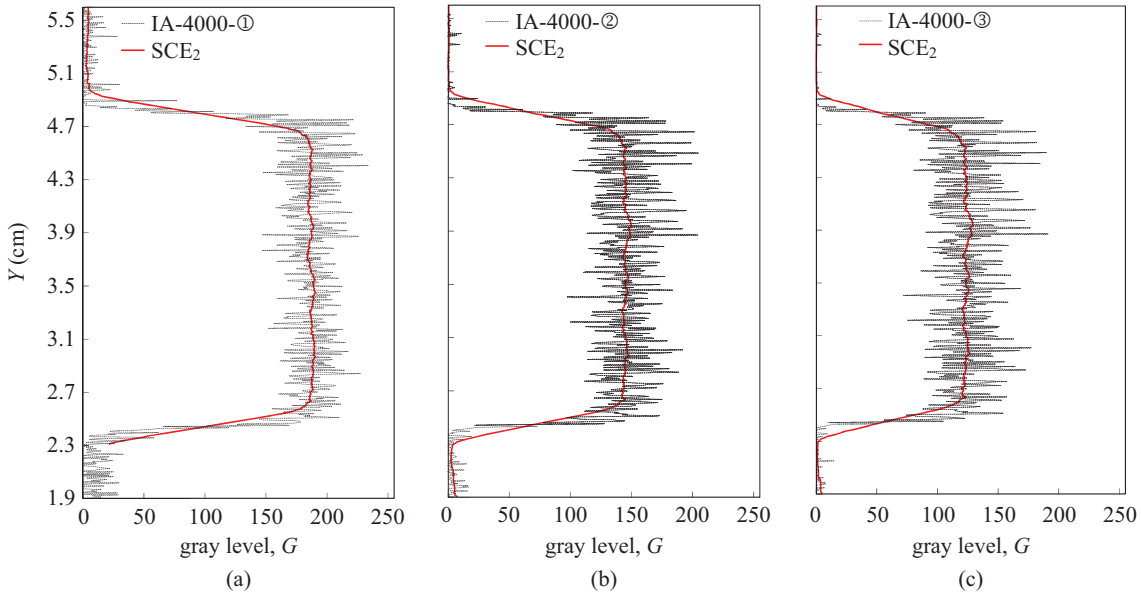

Fig. 12. Post-CE_2 gray level distributions obtained at X = 7.27 cm, together with display of SCE_2 counterparts with (a) IA-4000-①; (b) IA-4000-②; (c) IA-4000-③ manipulations

in Figs. 10(a) and (b) are presented in Fig. 10(c) with a combination of IA-4000-①, IA-4000-②, IA-4000-③ and IA-9000-① manipulations. With reference to the specified gray level of 15 shown in Figs. 10(a) and (b), the transformed counterparts corresponding to these peak probabilities for the water phase are equal to G_{Pi} (with $i = 1 \sim 4$) = 186, 144, 122 and 186, respectively, implying that the larger the value of G_{Pi} the lighter the image. Using the first three IA manipulations centering on G_{Pi} ($i = 1 \sim 3$), Figs. 11(a)-(c) present in order such secondly contrast-enhanced (hereafter termed "CE_2") editions of the CE_1-EA image for 4000-frame case, indicating remarkable contrast enhancement of the image for the free jet as compared with that shown in Fig. 9(a). These evidences do demonstrate that the larger the value of the enhanced gray-level, the lighter (or the more contrast-enhanced) the image of the free jet. Further, a comparison of the histograms between IA-4000-① and IA-9000-① as depicted in Fig. 10(d) reveals that these two peak probabilities corresponding to the identical gray level of 186 (= $G_{IA\text{-}P1} = G_{IA\text{-}P4}$) are 0.0134 and 0.0125. Note that the histogram having larger/smaller peak probability is accompanied by smaller/greater gray-level extension due to the sum of all probabilities is equal to unity (Johnson et al., 2011).

In addition, the ***CE_2 grey level distributions*** along the identical line at X = 7.27 cm are illustrated correspondingly in Figs. 12(a)-(c) for the 4000-frame images. It is worth mentioning that the CE_2 gray level distribution of using N (= 5000 ~ 9000) frames are similar to that of 4000 frames, i.e., these distributions are still evidenced to fluctuate with many spikes but having smaller fluctuating levels for increasing N (not shown). A symmetric smoothing scheme using a total of 51 points located at continuously different Y positions (i.e., also corresponding to successively different pixel positions, with 25 points both in the front and rear of the targeted pixel position) is adopted to smooth the CE_2 gray level fluctuations, aiming to obtain the smoothed

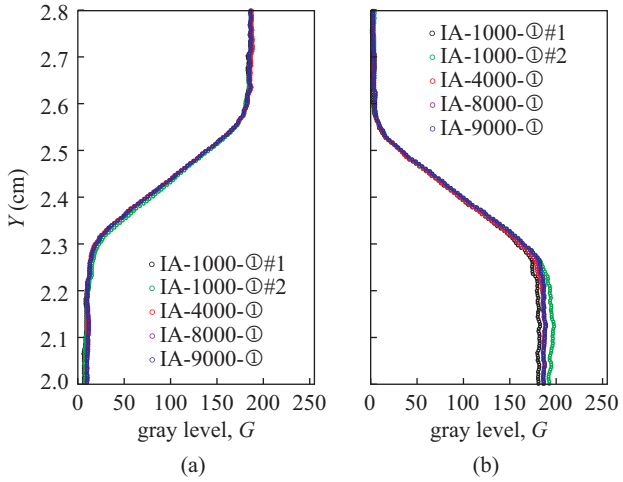

Fig. 13. Comparison of SCE_2 gray level distributions obtained at X = 7.27 cm for a total of N = 1000, 4000, 8000 and 9000 frames used in the neighborhood of (a) lower free surface; (b) upper free surface of free jet with IA-N-① manipulations (all centering on $G = G_{p1} = G_{p4} = 186$)

CE_2 (hereafter named "***SCE_2***") ***gray level distribution*** for a N-frame case. The SCE_2 gray level distributions associated with these three $G_{IA\text{-}Pi}$ (i = 1 ~ 3) values are also presented in Figs. 12(a)-(c). Due to the distinction in the values of G_{Pi}, the averaged values of the top-hats in the SCE_2 gray level distributions are also different and equal to 186.6, 144.3 and 122.1, respectively. Note that a very prominent gray-level gradient is clearly observed around the lower/upper free surface; and that a nearly constant distribution with very low gray level is also seen under/over the lower/upper free surface.

Figs. 13(a) and (b) show a series of the SCE_2 gray level distributions with N being varied from 1000 to 9000 near the lower/upper free surface within 2.00 cm ≤ Y ≤ 2.80 cm and 4.40 cm ≤ Y ≤ 5.20 cm, respectively. Two runs of the 1000-frame cases are also shown in Figs. 13(a) and (b) to highlight their evident distinctions and non-convergent feature. With increasing N, the entire trend of the SCE_2 gray level distribution for the N-frame case (with N = 1000 ~ 8000 and IA-N-① manipulations) is more toward that of the 9000-frame case. However, the SCE_2 gray level distributions of the 4000-frame and 8000-frame cases are nearly identical to that of the 9000-frame counterpart, strongly indicating fairly convergent situation with $N \geq 4000$.

Taking the 4000-frame image with G_{P1} = 186 (i.e., IA-4000-① manipulation) for example, all of the SCE_2 gray level distributions for $N \geq 4000$ at X = 7.27 cm do reveal some important features as illustrated below:

(1) A relatively uniform distribution having a gray level of $G_{lo,\,jet} \sim G_{up,\,jet}$ = 186.16 ~ 187.79 (with a mean value of 186.6) for about 2.60 cm ≤ Y ≤ 4.60 cm can be interpreted as the representative gray levels for "*each appearance of water phase*" from the free jet.
(2) A relatively uniform distribution with the gray level of $G_{lo,\,air}$ = 8.34 or $G_{up,\,air}$ = 3.98 for the lower or upper outside-zone located within 1.7 cm ≤ Y ≤ 2.1 cm or 5.0 cm ≤ Y ≤ 5.6 cm, highlight the typical gray level for "*each appearance of air phase*" from the air cavity or atmosphere.
(3) The lower or upper zone having evident *gray-level gradient* for about 2.1 cm ≤ Y ≤ 2.6 cm or 4.6 cm ≤ Y ≤ 5.0 cm, reflects the response of "*intermittent appearance of either water phase from the free jet or air phase from the air cavity or atmosphere*" because of high-frequency, irregular fluctuations in the free jet. Note that, along the water-air interface, each appearance of water phase would provide a gray level of $G_{lo,\,jet}$ or $G_{up,\,jet}$ and each show-up of air phase could contribute a gray level of $G_{lo,\,air}$ or $G_{up,\,air}$.
(4) Due to intermittent appearances of these two phases with random phase-switching on the water-air interfaces, the resulting SCE_2 gray levels should take the values of $[m \times G_{lo,\,jet} + (N - m) \times G_{lo,\,air}]/N$ and $[k \times G_{up,\,jet} + (N - k) \times G_{up,\,air}]/N$ for the lower and upper zones, respectively [with m and k being the times for intermittent appearance of water phase accompanied by $(N - m)$ and $(N - k)$ times for fitful show-up of air phase for $N \geq 4000$].
(5) During a statistical sampling, more intermittent appearances of water phase from the free jet within these two gradient zones would lead to the higher gray level. Such situation becomes more prominent/insignificant as the observation height (Y) is closer to/further away from the point exactly corresponding to full water phase from the free jet, thus constituting the lower and upper gray-level gradients between the air cavity and free jet as well as the free jet and atmosphere, respectively.

Further, at X = 7.27 cm, the global standard deviations of the SCE_2 gray level distributions for the N-frame cases (with N being varied from 1000, via 4000, up to 8000 and IA-N-① manipulation) with respect to that of the 9000-frame case are varied from 3.54, via 0.86, to 0.30, respectively (not shown). The trend clearly shows prominent decrease of the global standard deviation with increasing N. Note that the global standard deviation for the 4000-frame case is 0.86, less than a gray level of unity. The corresponding "coefficient of variation" (Johnson et al., 2011), defined as the ratio of the global standard deviation to a representative mean gray level, is equal to 0.46% (= 0.86/186.6 < 0.5%), highlighting the SCE_2 gray level distribution of the 4000-frame case can be promisingly used as an acceptable criterion for convergence.

6. Curving Fitting to Smoothed Gray Level Distribution

The data of the lower and upper gradient zones of the SCE_2 gray level distributions for the 4000-frame case are presented in Figs. 13(a) and (b) at X = 7.27 cm for 2.0 cm ≤ Y ≤ 2.8 cm and 4.4 cm ≤ Y ≤ 5.2 cm, respectively. It has been found that both distributions obviously demonstrate very prominent "***gray-level gradients***" in these two zones and two fairly uniform distributions appear outside each of the zone. Taking the 4000-frame image with G_{P1} = 186 (i.e., IA-4000-① manipulation) for example, the lower zone has the gray level increasing from $G_{lo,\,air}$ = 8.34

Table 1. List of various parameters associated with regression coefficients, gray levels and *Y* positions for 4000-frame and 9000-frame cases with four distinct IA manipulations.

lower free surface						upper free surface					
N-frame image (with different IA manipulations)	IA-4000-①	IA-4000-②	IA-4000-③	IA-9000-①	average	*N*-frame image (with different IA manipulations)	IA-4000-①	IA-4000-②	IA-4000-③	IA-9000-①	average
G_{pi} (i = 1 ~ 4)	186	144	122	186		G_{pi} (i = 1 ~ 4)	186	144	122	186	
* $G_{lo,\ jet}$	186.16	143.30	121.71	186.61		* $G_{up,\ jet}$	187.79	145.12	123.03	186.60	
* $G_{lo,\ air}$	8.34	4.52	1.01	10.63		* $G_{up,\ air}$	3.98	0.47	0.12	3.07	
$\Delta G_1 = G_{lo,\ jet} - G_{lo,\ air}$	177.82	138.78	120.70	175.98		$\Delta G_2 = G_{up,\ jet} - G_{up,\ air}$	183.81	144.65	129.91	183.53	
C_1	88.98	69.45	60.51	88.05		C_1	91.98	72.48	65.05	91.71	
C_2	-8.34	-8.52	-8.43	-8.81		C_2	8.44	8.56	8.35	8.86	
C_3	20.30	20.45	20.62	21.48		C_3	-40.57	-40.70	-40.95	-42.58	
C_4	88.83	69.31	60.22	87.96		C_4	91.85	72.20	64.88	91.85	
R^2	0.998	0.997	0.997	0.998		R^2	0.998	0.997	0.997	0.998	
$Y_{lo,\ 99\%\ water}$ at 99%ΔG_1 (cm)	2.686	2.691	2.673	2.676	2.681	$Y_{up,\ 1\%\ water}$ at 1%ΔG_2 (cm)	5.064	5.059	5.051	5.045	5.055
$Y_{lo,\ 98\%\ water}$ at 98%ΔG_1 (cm)	2.655	2.659	2.649	2.646	2.652	$Y_{up,\ 2\%\ water}$ at 2%ΔG_2 (cm)	5.029	5.025	5.019	5.016	5.022
$Y_{lo,\ 97\%\ water}$ at 97%ΔG_1 (cm)	2.634	2.638	2.621	2.626	2.630	$Y_{up,\ 3\%\ water}$ at 3%ΔG_2 (cm)	5.007	5.002	4.995	4.996	5.000
$Y_{lo,\ 75\%\ water}$ at 75%ΔG_1 (cm)	2.500	2.505	2.488	2.499	2.498	$Y_{up,\ 25\%\ water}$ at 25%ΔG_2 (cm)	4.871	4.867	4.861	4.870	4.867
$Y_{lo,\ 50\%\ water}$ at 50 %ΔG_1 = $Y_{lo,\ hw}$ = $Y_{lo,\ in}$ (cm)	2.434	2.439	2.431	2.437	2.435	$Y_{up,\ 50\%\ water}$ at 50%ΔG_2 = $Y_{up,\ hw}$ = $Y_{up,\ in}$ (cm)	4.807	4.794	4.798	4.809	4.802
$Y_{lo,\ 25\%\ water}$ at 25%ΔG_1 (cm)	2.369	2.372	2.375	2.376	2.373	$Y_{up,\ 75\%\ water}$ at 75%ΔG_2 (cm)	4.743	4.738	4.732	4.749	4.741
$Y_{lo,\ 3\%\ water}$ at 3%ΔG_1 (cm)	2.235	2.239	2.243	2.255	2.243	$Y_{up,\ 97\%\ water}$ at 97%ΔG_2 (cm)	4.616	4.612	4.608	4.635	4.618
$Y_{lo,\ 2\%\ water}$ at 2%ΔG_1 (cm)	2.216	2.220	2.227	2.236	2.225	$Y_{up,\ 98\%\ water}$ at 98%ΔG_2 (cm)	4.598	4.591	4.588	4.621	4.600
$Y_{lo,\ 1\%\ water}$ at 1%ΔG_1 (cm)	2.183	2.190	2.198	2.213	2.196	$Y_{up,\ 99\%\ water}$ at 99%ΔG_2 (cm)	4.572	4.568	4.561	4.602	4.576

* Practical data, not fitted values.

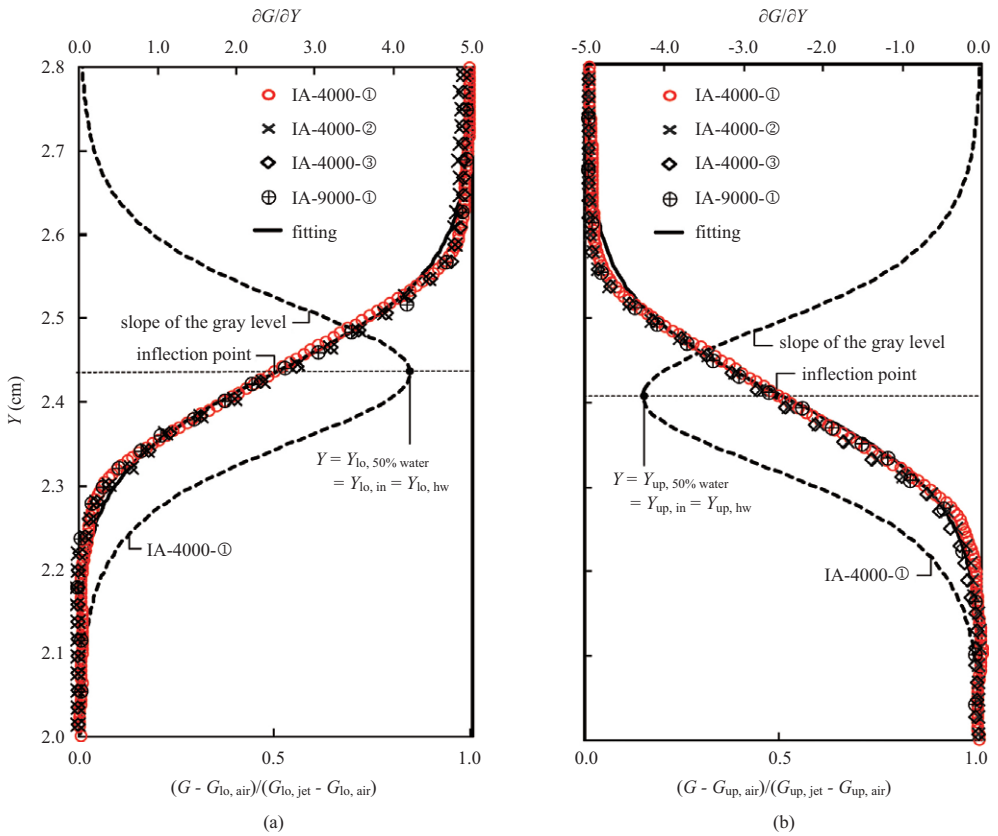

Fig. 14. Pronounced SCE_2 gray-level gradient prevailing in the neighborhood of (a) lower free surface; (b) upper free surface of free jet with four different IA manipulations.

for the lower air region to $G_{lo,\,jet} = 186.16$ for the lower part of free jet; and the upper zone holds the counterpart decreasing from $G_{up,\,jet} = 187.79$ to $G_{up,\,air} = 3.98$. Accordingly, nonlinear curve fittings to the data of the SCE_2 gray level distributions were performed. The equation representing the regressed gray level, $G(Y)$, can be expressed as

$$G(Y) = C_1 \times \tanh\left(C_2 Y + C_3\right) + C_4 \tag{1}$$

in which C_1, C_2, C_3 and C_4 are regression coefficients for the lower and upper zones of the fitted gray level distributions, respectively. The values of $C_1 \sim C_4$ for distinct IA manipulations are listed in Table 1.

Figs. 14(a) and (b) show fairly good agreement between the data corresponding to the four G_{Pi} ($i = 1 \sim 4$) and the fits at $X =$ 7.27 cm for the 4000-frame and 9000-frame cases. It is surprisingly found that a unified gray-level gradient zone exists between two dimensionless uniform gray-levels of full air and water phases around the lower or upper free surface. Namely, if re-scaling of the differences in the gray levels ($G - G_{lo,\,air}$) and ($G - G_{up,\,air}$) with respect to the characteristic gray-level scale ($G_{lo,\,jet} - G_{lo,\,air}$) and ($G_{up,\,jet} - G_{up,\,air}$) is performed, respectively, it is unexpectedly found that no influence of the IA manipulations with different G_{Pi} ($i = 1 \sim 4$) values on the dimensionless gray level distribution. For easy comprehension, a list for summarizing key variables associated with these IA manipulations is also given in Table 1. After thorough examinations performed not only at different positions for the identical 4000-frame case, but also at the same position having different N-frame cases ($N =$ 5000 ~ 9000) or even at distinct locations and for different N-frame cases, the statements made above is still valid, however the values of these regression coefficients are subject to change. Therefore, the illustrations made in the following will be mainly focused on the 4000-frame case with the IA-① manipulation.

7. Probabilistic Mean Positions for Lower and Upper Free Surface Profiles of Free Jet

Up to now, it is pertinent to re-mention that very random, high-frequency fluctuations moving up and down both temporally and spatially exist on the free surface elevations and profiles of the free jet. Therefore, *the probabilistic mean position of the free surface elevation of free-jet should vary with the definition of how many percentages* of *the intermittent appearance of water phase occurring at an identified location*. Herein, say I% ($= N_{w1}/N_{t1}$) meaning that the intermittent appearance of water phase takes place N_{w1} times in the N_{t1}-frame images. Given that the representative mean gray level for each appearance of water phase at $X = 7.27$ cm for $N_{t1} = 4000$ is equal to a gray level of $G_{lo,\,jet} = 186.16$ or $G_{up,\,jet} = 187.79$; and that the counterpart for air phase is identified as $G_{lo,\,air} = 8.34$ or $G_{up,\,air} = 3.98$, respectively. It can be generally recognized that the ***mean positions*** of the lower and upper free surfaces of the free jet occur intermittently about 2000 times in the 4000-frame images (i.e., equivalently with a time portion of 50% appearance), thus leading to the resulted gray levels equal to $(G_{lo,\,jet} + G_{lo,\,air})/2 = 97.25$ and $(G_{up,\,jet} + G_{up,\,air})/2 = 95.89$, respectively.

Based on such kind of gray-level gradient feature (behaving similarly like a traditional velocity gradient), this principle is used to determine the *probabilistic mean positions* of the following interfaces:

(1) Nearly full air phase beneath the lower free surface of free jet (i.e., with at least 97% appearance of air phase from the air cavity or at most 3% appearance of water phase from the free jet for the lower zone);
(2) Intermittent switching of water-air interface for the lower zone with 50% appearance of water phase accompanied by 50% show-up of air phase from the air cavity;
(3) Almost full water phase for the lower free surface of free jet (i.e., with at least 97% appearance of water phase or at most 3% appearance of air phase from the air cavity);
(4) Nearly full water phase for the upper free surface of free jet (i.e., with at least 97% appearance of water phase from the free jet or at most 3% appearance of air phase from the atmosphere);
(5) Intermittent switching of water-air interface for the upper zone with 50% appearance of water phase accompanied by 50% show-up of air phase from the atmosphere; and
(6) Almost full air phase (i.e., with at least 97% appearance of air phase from the atmosphere or at most 3% appearance of water phase from the free jet for the upper zone).

Since the regression equations of the SCE_2 gray level distributions $G(Y)$ have been obtained, it is very easy to acquire the first derivative of the fitted gray level with respect to Y, i.e., the slope of the gray level, $\partial G/\partial Y$. For simplicity, only the plots of $\partial G/\partial Y$ at $X = 7.27$ cm for IA-4000-① manipulation are presented in Figs. 14(a) and (b). The maximum value of $\partial G/\partial Y$ occurs right at a specified height where the *inflection point* (Lin et al., 2008b) is located, i.e., $Y = Y_{lo,\,in}$ (= 2.434 cm) for the lower gradient zone or $Y = Y_{up,\,in}$ (= 4.807 cm) for the upper gradient zone. After detailed checks and comparisons, it is surprisingly found that the height of the inflection point, $Y_{lo,\,in}$ or $Y_{up,\,in}$, is exactly equivalent to the height of the "*half-width*" of the gradient zone, i.e., $Y = Y_{lo,\,hw}$ or $Y = Y_{up,\,hw}$, where the fitted gray level exactly equal to $(G_{lo,\,jet} + G_{lo,\,air})/2 = 97.25$ or $(G_{up,\,jet} + G_{up,\,air})/2 = 95.89$ in the lower or upper gradient zone, respectively. Accordingly, this specified position located at $Y = Y_{lo,\,hw}/Y = Y_{up,\,hw}$ for the lower/upper gradient zone can be reasonably rendered as the customary ***mean position*** of the interface with 50% intermittent appearance of water phase from the free jet accompanied by 50% fitful show-up of air phase from the air cavity/atmosphere. Namely, $Y = Y_{lo,\,50\%\,water} = Y_{lo,\,in} = Y_{lo,\,hw} = 2.434$ cm and $Y = Y_{up,\,50\%\,water} = Y_{up,\,in} = Y_{up,\,hw} = 4.807$ cm (see Table 1 for IA-4000-① manipulation). Similarly, the corresponding results for IA-4000-②, IA-4000-③ and IA-9000-① manipulations are also shown in Table 1, indicating that the values of customary mean position are almost identical with respect to the averaged one and nearly no influence of different IA manipulations on determining these specified positions.

Further, two characteristic gray-level scales for the lower and upper gradient zones of the fitted gray level distribution are defined as $\Delta G_1 = (G_{lo,\,jet} - G_{lo,\,air})$ or $\Delta G_2 = (G_{up,\,jet} - G_{up,\,air})$, respectively. For the steady laminar boundary layer over a thin flat plate, the boundary layer thickness (in which the velocity gradient exists) could be defined as the specified height measured from the flat plate up to the edge of boundary layer where the velocity is equal to (0.970 ~ 0.990) times the free-stream uniform velocity (Yuan, 1967; Schlichting, 1979). Following the similar way, the locations at which the fitted gray levels for the lower gradient zone have the values of at most (3% × ΔG_1) are defined as the representative interfaces with almost full air (i.e., at least 97% appearance of air phase or at most 3% appearance of water phase) for the lower zone, i.e., $Y_{lo,\,97\%\,air} \sim Y_{lo,\,99\%\,air}$ (or $Y_{lo,\,3\%\,water} \sim Y_{lo,\,1\%\,water}$). Furthermore, the counterparts that have the values of at least (97.0% × ΔG_1) are considered as the interfaces with nearly full water (i.e., at least 97% appearance of water phase) for the lower zone, $Y_{lo,\,97\%\,water} \sim Y_{lo,\,99\%\,water}$ (or $Y_{lo,\,3\%\,air} \sim Y_{lo,\,1\%\,air}$). Similarly, the positions for the counterparts of the upper gradient zone with the values of at least (97% × ΔG_2) and at most (3.0% × ΔG_2) are characterized as the typical interfaces with almost full water (i.e., at least 97% appearance of water phase or at most 3% of air phase) $Y_{up,\,97\%\,water} \sim Y_{up,\,99\%\,water}$ (or $Y_{up,\,3\%\,air} \sim Y_{up,\,1\%\,air}$); and with nearly full air (i.e., at most 3% appearance of water phase), $Y_{up,\,3\%\,water} \sim Y_{up,\,1\%\,water}$ (or $Y_{up,\,97\%\,air} \sim Y_{up,\,99\%\,air}$).

A summarized table for various representative heights at X = 7.27 cm is also presented in Table 1 for 4000-frame and 9000-frame cases (with all IA manipulations). It is surprisingly found that all of these representative heights and corresponding gray levels for different N_t-frame cases (with N_{t1} = 4000 and N_{t2} = 9000) are nearly the same only with very tiny differences. For example, the values of $Y_{lo,\,98\%\,air}$ or $Y_{lo,\,2\%\,water}$ for the 4000-frame and 9000-frame (with IA-4000-① and IA-9000-① manipulations) cases are 2.216 cm and 2.236 cm; and the counterparts of $Y_{up,\,98\%\,water}$ (or $Y_{up,\,2\%\,air}$) are 4.598 cm and 4.621 cm, respectively. The relative errors with respect to the mean values are less than 0.49% and 0.46% for the lower and upper free surfaces, respectively. It is also worth re-mentioning that, as clearly witnessed in Figs. 14(a) and (b) and Table 1, various representative heights obtained at X = 7.27 cm for 4000-frame and 9000-frame cases with distinct IA manipulations are almost the same.

By similar analysis for different X positions, the three lower lines of the $Y_{lo,\,3\%\,water}$, $Y_{lo,\,50\%\,water}$ and $Y_{lo,\,97\%\,water}$ as well as the three upper lines of the $Y_{up,\,97\%\,water}$, $Y_{up,50\%\,water}$ and $Y_{up,\,3\%\,water}$ can be identified for the free jet by using any one of the five datasets (because of very tiny differences among the values of these specified heights with four distinct IA manipulations together with the averaged data) and presented in Fig. 15 for 3.95 cm ≤ X ≤ 9.15 cm. The lower $Y_{lo,\,50\%\,water}$ and higher $Y_{up,\,50\%\,water}$ are approximately along the interface where the gradient of SCE_2 gray level distribution is very prominent and situated between the bright and dark zones, which represent the free jet and air, respectively. Due to precise determination of these points on the representative lines, all the points on these lines along the interfaces in-

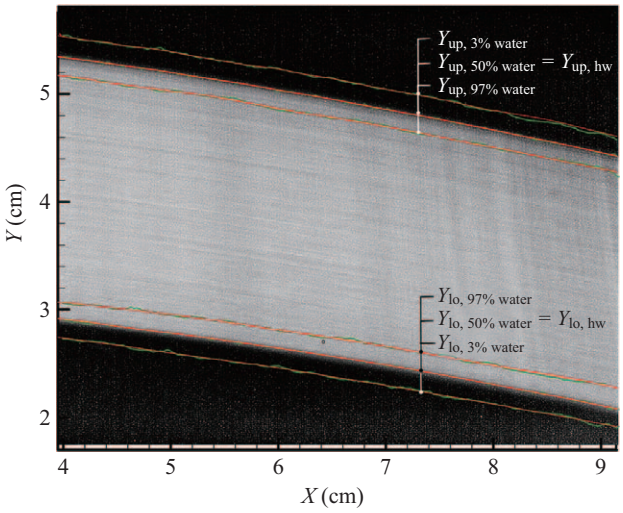

Fig. 15. Plotting of both three lower lines for $Y_{lo,\,3\%\,water}$, $Y_{lo,\,50\%\,water}$ and $Y_{lo,\,97\%\,water}$ and three upper lines for $Y_{up,\,97\%\,water}$, $Y_{up,\,50\%\,water}$ and $Y_{up,\,3\%\,water}$, together with illustration of CE_2 image with IA-9000-① manipulation.

evitably exhibit a certain degree of tiny fluctuation. A moving average technique is therefore adopted by using symmetric scheme to smooth these representative lines. Finally, the post-smoothing lower and upper three lines are obtained and shown also in Fig. 15.

8. Instantaneous and Probabilistic Mean Velocity Fields of Free Jet

An instantaneous velocity field obtained for -0.21 cm ≤ X ≤ 4.63 cm using HSPIV is shown in Fig. 16(a), along with exhibition of two sets of the three representative lines. Note that all the lower three lines for $Y_{lo,\,3\%\,water}$, $Y_{lo,\,50\%\,water}$ and $Y_{lo,\,97\%\,water}$ are convergent and completely overlapped at (X, Y) = (0, 3.2) cm. In Fig. 16(a), each velocity vector plotted either between the lower $Y_{lo,\,3\%\,water}$ and $Y_{lo,\,97\%\,water}$ or between the upper $Y_{up,\,97\%\,water}$ and $Y_{up,\,3\%\,water}$ truly reflects the instantaneous existence of water flow from the free jet. Some parts of the instantaneous velocity profiles are not uniform due to high-speed free jet with turbulent nature (Vischer and Hager, 1995). For the lower part, *almost all* of the velocity vectors are not present in the instantaneous velocity fields due to "intermittent absence" of water flow especially inside the zone between $Y_{lo,\,3\%\,water}$ and $Y_{lo,\,50\%\,water}$. For the upper part, the velocity vectors are *partially* and *mostly* absent between $Y_{up,\,97\%\,water}$ and $Y_{up,\,50\%\,water}$ as well as between $Y_{up,\,50\%\,water}$ and $Y_{up,\,3\%\,water}$, respectively, demonstrating the feature of prominent free surface fluctuation in the free jet. Further, an instantaneous velocity field measured for 4.10 cm ≤ X ≤ 8.94 cm is presented in Fig. 16(b), from which *most* of the velocity vectors in the lower part are lacking in the instantaneous velocity field due to fitful absence of water flow between $Y_{lo,\,3\%\,water}$ and $Y_{lo,\,50\%\,water}$. On the other hand, for the upper part, the velocity vectors are *completely and partially* absent between the upper $Y_{up,\,50\%\,water}$ and $Y_{up,\,3\%\,water}$ as well as between the upper $Y_{up,\,97\%\,water}$ and $Y_{up,\,50\%\,water}$, exhibiting again the characteristics

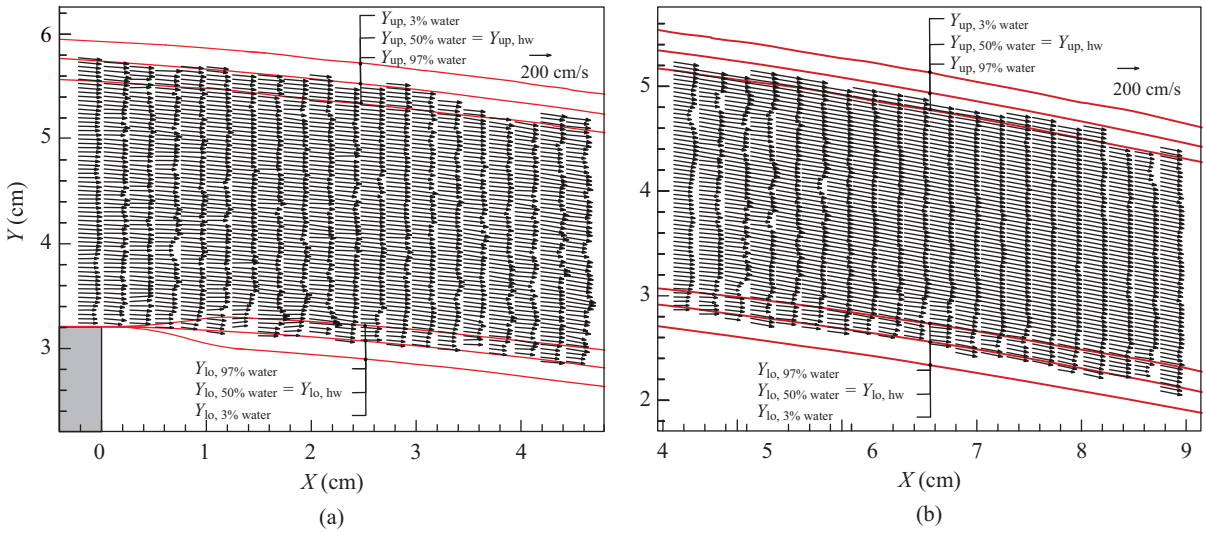

Fig. 16. Two instantaneous velocity fields for (a) -0.21 cm ≤ X ≤ 4.63 cm; (b) 4.10 cm ≤ X ≤ 8.94 cm.

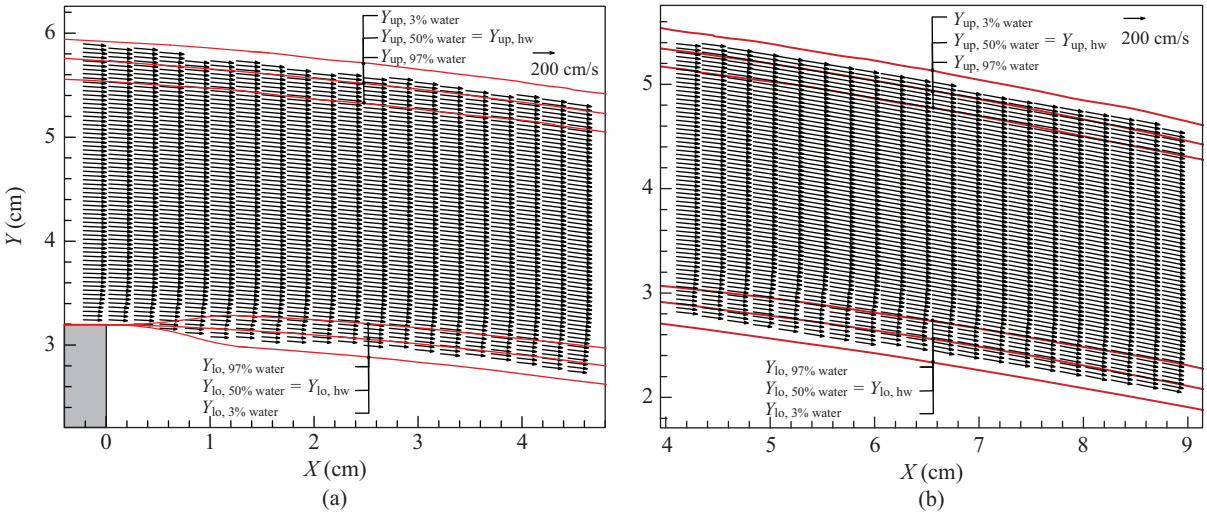

Fig. 17. Two conditionally time-averaged velocity fields for (a) -0.21 cm ≤ X ≤ 4.63 cm; (b) 4.1 cm ≤ X ≤ 8.94 cm.

of prominent fluctuations in the free surface profiles of free jet. Figs. 17(a) and (b) illustrate the ***conditionally time-averaged*** velocity fields for -0.21 cm ≤ X ≤ 4.63 cm and 4.10 cm ≤ X ≤ 8.94 cm, respectively, with a conditional average of N_{w2}-frame images, which are identified to have the intermittent appearance of water phase N_{w2} times in the N_{t2}-frame images (N_{t2} = 9000). Note that, if the probability of water phase is equal to I% = N_{w2}/N_{t2}, the height of this specified point is surprisingly found to almost equal $Y = Y_{lo,\ I\%\ water}$ (or $Y_{lo,\ (100\text{-}I)\%\ air}$) or $Y = Y_{up,\ I\%\ water}$ (or $Y_{up,\ (100\text{-}I)\%\ air}$). Figs. 17(a) and (b) also highlight that each velocity profile is very uniform, except that the velocity distribution between $Y_{lo,\ 3\%\ water}$ and $Y_{lo,\ 97\%\ water}$ is slightly smaller than that for $Y > Y_{lo,\ 97\%\ water}$. Two of the further evidences around the *lower free surface* are presented in Figs. 18(a) and (b) with close-ups of the conditionally time-averaged velocity profiles obtained at X = 2.03 cm and X = 7.27 cm, respectively. This feature stems, in fact, from the non-slipping condition imposed on chute surface such that the velocities of the approaching flow right on the chute surface is 0 cm/s and evident velocity gradient exists within Y = 3.75 cm ~ 3.91 cm for -4.0 cm ≤ X ≤ 0 cm (see Fig. 4). As seen in Figs. 17(a) and (b), once the approaching flow exactly leaves the brink of the offset and the free jet starts to commence immediately downstream of X = 0 cm, the velocity distribution around the lower free surface should be smaller than that of the upper one which has very uniform profile. In addition, Figs. 19(a) and (b) present close-ups of the conditionally time-averaged velocity profile around the upper free surface measured at X = 2.03 cm and X = 7.27 cm, respectively, again demonstrating that very uniform velocity distribution existing very close to the free surface for the conditionally time-averaged velocity fields.

In addition, Figs. 20(a) and (b) show the ***overall time-averaged***

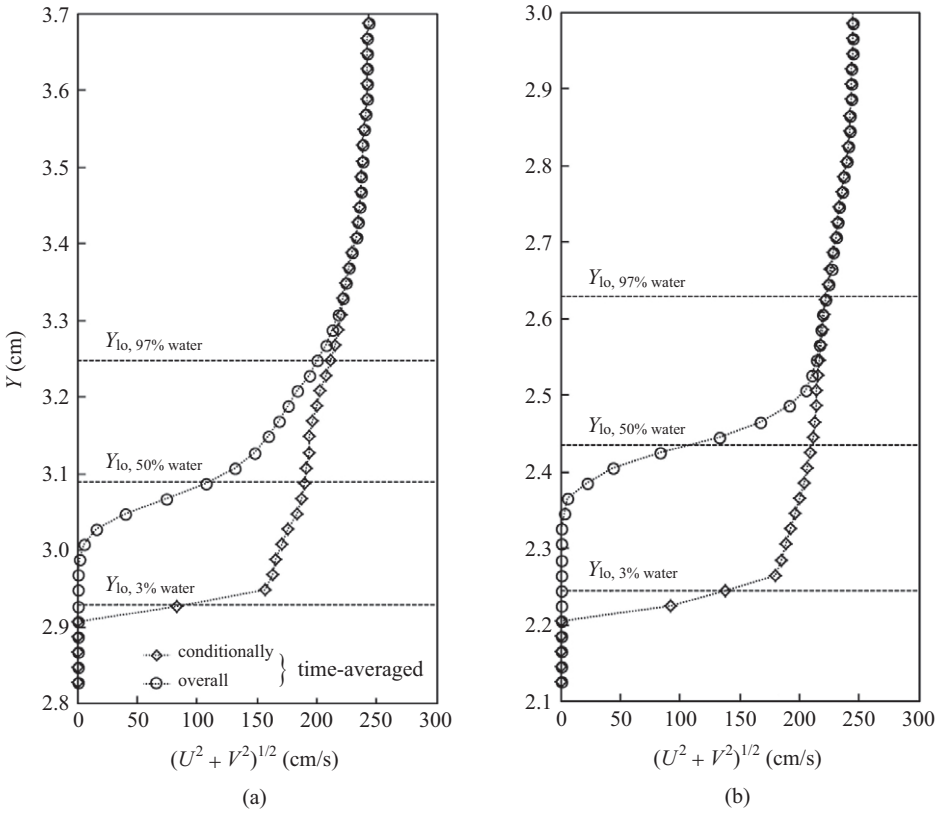

Fig. 18. Close-ups of both conditionally and overall time-averaged velocity profiles of free jet near lower free surface (a) at $X = 2.03$ cm; (b) at $X = 7.27$ cm.

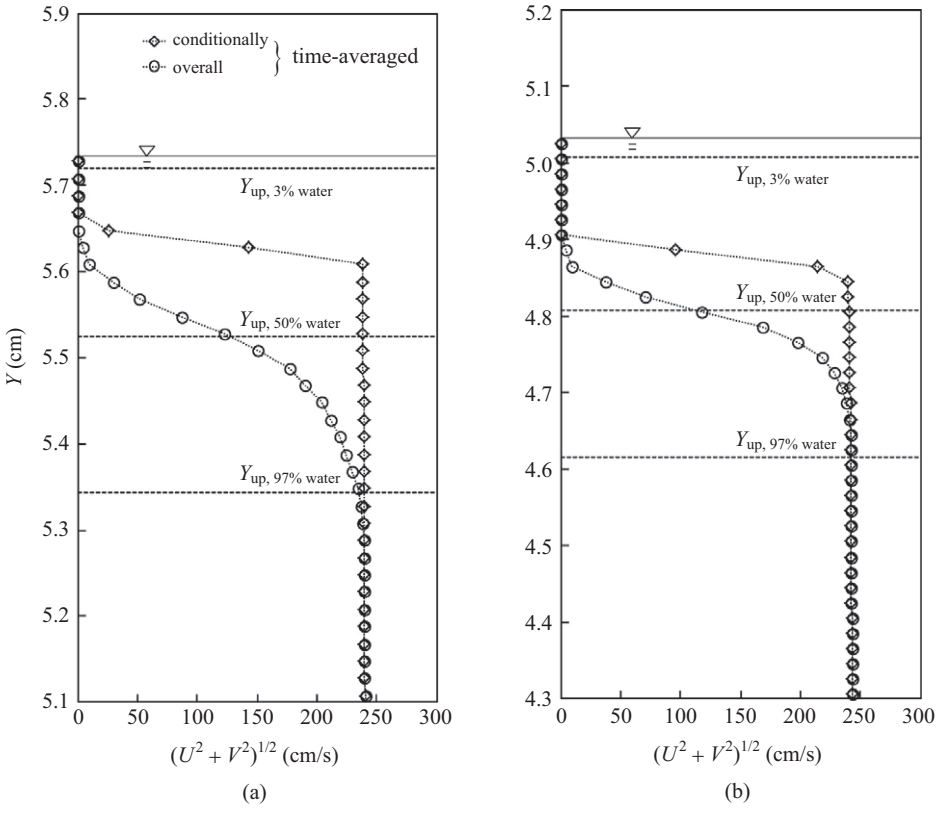

Fig. 19. Close-ups of both conditionally and overall time-averaged velocity profiles of free jet near upper free surface (a) at $X = 2.03$ cm; (b) at $X = 7.27$ cm.

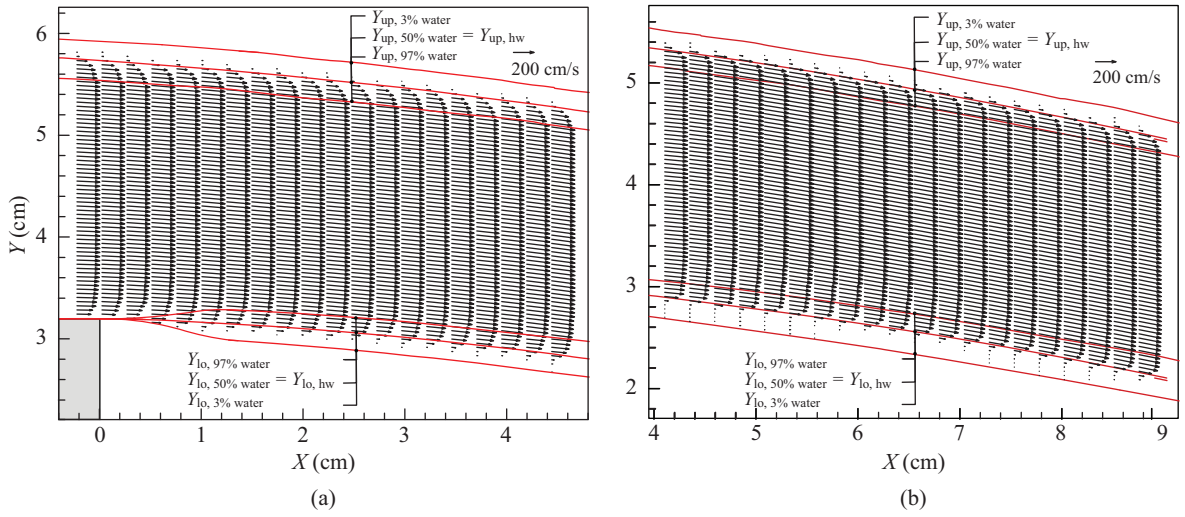

Fig. 20. Two overall time-averaged velocity fields for (a) -0.21 cm ≤ X ≤ 4.63 cm; (b) 4.1 cm ≤ X ≤ 8.94 cm.

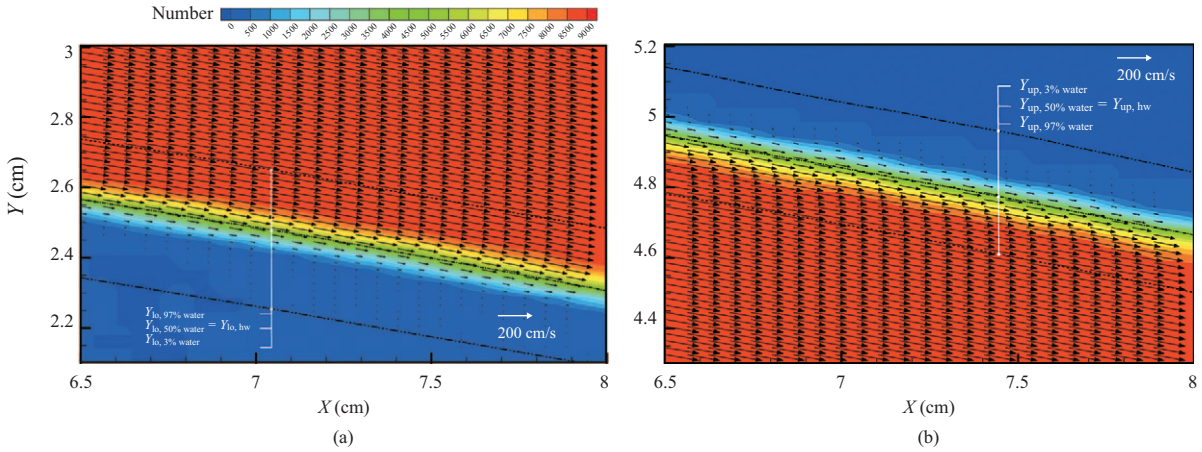

Fig. 21. Magnified view of overall time-averaged velocity field of free jet near (a) lower free surface; (b) upper free surface for 6.5 cm ≤ X ≤ 8.0 cm, together with distribution of occurrence times for water phase using a total of 9000 frames

velocity fields for -0.21 cm ≤ X ≤ 4.63 cm and 4.10 cm ≤ X ≤ 8.94 cm with an ensemble-average of 9000 images. For the flow regions between $Y_{lo,\ 97\%\ water}$ and $Y_{up,\ 97\%\ water}$, each mean velocity distribution having a *characteristic uniform velocity* of $(U^2 + V^2)^{1/2}$ is nearly same as the counterpart in Figs. 17(a) and (b). However, each velocity distribution either in the lower part between $Y_{lo,\ 3\%\ water}$ and $Y_{lo,\ 97\%\ water}$ or in the upper part between $Y_{up,\ 97\%\ water}$ and $Y_{up,\ 3\%\ water}$ obviously exhibits non-uniform feature with prominent velocity gradient. Such kind of detailed velocity gradients in the lower and upper parts for 6.5 cm ≤ X ≤ 8.0 cm can be further witnessed by using magnified views of the velocity field, as seen in Figs. 21(a) and (b). Close-ups of the overall time-averaged velocity profiles obtained at X = 2.03 cm and X = 7.27 cm for the lower/upper part of the free surface are shown in Figs. 18(a) and (b)/Figs. 19(a) and (b), respectively. It is interestingly found that the distinction between the two velocity profiles and the corresponding difference in the unit discharges, which are obtained by conditionally and overall time-averaged methods, for the lower part is more prominent and larger than that for the upper part, respectively.

The probability distribution corresponding to the intermittent appearance of water phase N_w times in the 9000 images is also displayed with different colors in Figs. 21(a) and (b) for the lower and upper parts, respectively. After a series of detailed checks for the relationship between $Y_{lo,\ I\%\ water}$ or $Y_{up,\ I\%\ water}$ and the lower or upper part of the probability distribution, it is surprisingly found that the values of $Y_{lo,\ I\%\ water}$ (or $Y_{lo,\ (100\ -\ I)\%\ air}$) and $Y_{up,\ I\%\ water}$ (or $Y_{up,\ (100\ -\ I)\%\ air}$) on the representative lines are almost the same as those obtained by the probability distribution corresponding to the intermittent appearance of water phase N_w times in the 9000 images. For example, for the positions on the line of either $Y_{lo,\ 50\%\ water}$ or $Y_{up,\ 50\%\ water}$, the intermittent appearances of water phase are identified to be 4445 ~ 4555 or 4460 ~ 4541 times (both having a mean value of 4500 times) in the 9000 images, further demonstrating that the position at which the probability of the intermittent appearance of water phase

Table 2. List of variables associated with probabilistic mean positions for upper and lower free surfaces, net depth, cross-sectional averaged resultant velocity and unit discharge of free jet for 0 cm ≤ X ≤ 8.5 cm.

X (cm)	$Y_{up,\,3\,\%\,water}$ (cm)	$Y_{lo,\,3\%\,water}$ (cm)	$[h(X)]_{up\text{-}lo,\,3\%\,water}$ (cm)	$[\overline{V}\,(X)]_{up\text{-}lo,\,3\%\,water}$ (cm/s)	$[q(X)]_{up\text{-}lo,\,3\%\,water}$ (cm^2/s)	$[q_{ave}]_{up\text{-}lo,\,3\%\,water}$ (cm^2/s)
	(1)	(2)	(3) = (1) – (2)	(4)	(5) = (3) × (4)	(6)
0.00	5.93	3.20	2.73	209.60	572.21	572.20
2.03	5.72	2.89	2.83	202.10	571.96	
3.54	5.59	2.78	2.81	203.58	572.06	
4.51	5.30	2.51	2.79	205.10	572.23	
6.02	5.22	2.45	2.77	206.50	572.01	
7.27	5.00	2.24	2.76	207.58	572.93	
8.51	4.76	2.03	2.73	209.80	572.02	

equal to 50% is located exactly along the line of either $Y_{lo,\,50\%\,water}$ or $Y_{up,\,50\%\,water}$.

Finally, a check for *continuity* between the approaching flow and free jet is performed. It should be specially mentioned that, by employing similar analysis for the probabilistic mean position for the free surface of the approaching flow, the "mean" and "additional" unit discharges exists below and beyond the specified height $Y_{50\%\,water}$ are $[q_{app}]_{50\%\,water}$ = 562.6 cm^2/s and $[q_{app}]_{50\%\sim3\%\,water}$ = 9.55 cm^2/s, respectively. Note that, for the free jet, $Y_{lo,\,50\%\,water}$ and $Y_{up,\,50\%\,water}$ can be generally regarded as the customary mean positions of the lower and upper free-surface elevations. As shown in Table 2, the values of $Y_{lo,\,3\%\,water}$, $Y_{up,\,3\%\,water}$, the net depth $[h(X)]_{up\text{-}lo,\,3\%\,water}$ (= $Y_{up,\,3\%\,water} - Y_{lo,\,3\%\,water}$), the cross-sectional averaged resultant velocity $[\overline{V}\,(X)]_{up\text{-}lo,\,3\%\,water}$ and the unit discharge $[q(X)]_{up\text{-}lo,\,3\%\,water}$ (= $[h(X)]_{up\text{-}lo,\,3\%\,water} \times [\overline{V}\,(X)]_{up\text{-}lo,3\%\,water}$) are listed for seven specified locations ranging from X = 0 cm to X = 8.51 cm. It is found that the values of $[q(X)]_{up\text{-}lo,\,3\%\,water}$ range from 571.96 cm^2/s to 572.93 cm^2/s with the averaged value of $[q_{ave}]_{up\text{-}lo,\,3\%\,water}$ = 572.20 cm^2/s. The relative errors of the unit discharges with respect to the averaged value are less than 0.13%. Next, the magnitudes of $[q(X)]_{up\text{-}lo,\,50\%\,water}$ vary from 561.44 cm^2/s to 562.31 cm^2/s with the averaged value of $[q_{ave}]_{up\text{-}lo,\,50\%\,water}$ = 561.96 cm^2/s being nearly identical to $[q_{app}]_{50\%\,water}$ = 562.6 cm^2/s. Further, the value of $\{[q(X)]_{lo,\,3\%\sim50\%\,water} + [q(X)]_{up,\,50\%\sim3\%\,water}\}$ change from 10.16 cm^2/s to 10.79 cm^2/s with an averaged value of $\{[q_{ave}]_{lo,\,3\%\sim50\%\,water} + [q_{ave}]_{up,\,50\%\sim3\%\,water}\}$ = 10.52 cm^2/s for 0 cm ≤ X ≤ 8.51 cm (not shown), demonstrating the contribution of unit discharge from the two thin layers ranging between $Y_{lo,\,3\%\,water}$ and $Y_{lo,\,50\%\,water}$ as well as between $Y_{up,\,50\%\,water}$ and $Y_{up,\,3\%\,water}$. Finally, the total unit discharges of the approaching flow and free jet are $\{[q_{app}]_{50\%\,water} + [q_{app}]_{50\%\sim3\%\,water}\}$ = 572.15 cm^2/s and $\{[q_{ave}]_{lo,\,3\%\sim50\%\,water} + [q_{ave}]_{up\text{-}lo,\,50\%\,water} + [q_{ave}]_{up,\,50\%\sim3\%\,water}\}$ = 572.48 cm^2/s, respectively, indicating both almost the same only with extremely tiny difference. These witnesses strongly confirm the continuity between the approaching flow and free jet and clearly highlight very precise measurements of HSPIV and fine determination of the $Y_{lo,\,I\%\,water}$ and $Y_{up,\,I\%\,water}$ positions.

IV. CONCLUDING REMARKS

In the present study, an optic-based method employing the particle-laden images taken during the HSPIV measurements has been used to explore the characteristics of free jet having high-frequency random fluctuations. A target experiment with a supercritical approaching flow has been performed to realize this method. Determination of the probabilistic mean positions for the lower or upper free surface profile (with the water-air interface having I% intermittent appearance of water phase accompanied by (100 – I)% fitful show-up of air phase) is elucidated in detail using the fitted grey-level gradients. It is surprisingly found that there is no influence of the imadjust (IA) with histogram specifications on the dimensionless gray level distributions and associated probabilistic mean positions of the lower and upper free surface elevations.

Two sets of three representative lines of $Y_{lo,\,3\%\,water}$, $Y_{lo,\,50\%\,water}$ and $Y_{lo,\,97\%\,water}$ as well as $Y_{up,\,97\%\,water}$, $Y_{up,\,50\%\,water}$ and $Y_{up,\,3\%\,water}$, which highlight different probabilistic mean positions of the lower and upper free-surface elevations of the free jet, have been demonstrated, respectively. It has also been shown that the values of $Y_{lo,\,I\%\,water}$ and $Y_{up,\,I\%\,water}$ on these representative lines which are determined by the fitted gray-level gradients are almost the same as those obtained by the probability distribution corresponding to the intermittent appearance of water phase N_{w1} times in the N_{t1}-frame images (i.e., I% = N_{w1}/N_{t1} with N_{t1} = 4000 for the free surface profiles). Further, the "probabilistic mean" velocity field has been mainly classified into: (1) the *conditionally time-averaged* one with a conditional ensemble-average of N_{w2}-frame images (which are identified to possess the intermittent appearance of water phase N_{w2} times in the N_{t2}-frame images and thus have the probability of I% = N_{w2}/N_{t2} with N_{t2} = 9000 for the velocity fields); and (2) the *overall time-averaged* one with an ensemble-average of all the N_{t2}-frame images. Each velocity profile $U(Y)$ in the conditionally time-averaged velocity field is fairly uniform, except that the velocity distribution in the lower part between $Y_{lo,\,3\%\,water}$ and $Y_{lo,\,97\%\,water}$ within which the velocity distribution is relatively uniform but with smaller magnitude of velocity. However, for the overall time-averaged velocity field, each velocity distribution either in the lower part between $Y_{lo,\,3\%\,water}$ and $Y_{lo,\,97\%\,water}$ or in the upper part between $Y_{up,\,97\%\,water}$ and $Y_{up,\,3\%\,water}$ evidently shows the non-uniform feature with significant velocity gradient. Finally, a check for

continuity between the approaching flow and free jet has been performed to confirm the mass conservation between the approaching flow and free jet and to demonstrate very precise measurements of HSPIV and accurate determination of both $Y_{lo,\, I\%\ water}$ and $Y_{up,\, I\%\ water}$ positions.

It is expected that this method can be applied to various flow fields with *air-liquid interface* having high-frequency random fluctuation, along with seeding particles being provided for liquid flow and air stream. Simultaneous measurements of the instantaneous and "probabilistic mean" momentum exchanges associated with mass or heat transfer can be explored in the vicinity of the interface having I% intermittent appearance of liquid phase followed by (100 – I)% fitful show-up of air phase.

ACKNOWLEDGEMENTS

The study presented here was carried out as part of a Ph. D. project "Hydraulic design of chute spillway aerators", funded by Swedish Hydropower Centre (SVC). SVC has been established by the Swedish Energy Agency (Energimyndigheten), Energiforsk AB and Svenska Kraftnät together with Royal Institute of Technology (KTH), Luleå University of Technology (LTU), Chalmers University of Technology (CHT) and Uppsala University (UU), with the website of www.svc.nu. The authors are indebted to Ms. Sara Sandberg of SVC and Ms. Maria Bartsch of Svenska Kraftnät for project co-ordinations.

REFERENCES

Adrain, R. J. and J. Westerweel (2011). Particle Image Velocimetry. Cambridge University Press, New York, USA.

Bennett, S. J. and C. V. Alonso (2006). Turbulent flow and bed pressure within headcut scour holes due to plane reattached jets. Journal of Hydraulic Research, IAHR, 44(4), 510-521.

Chamani, M. R. and M. K. Beirami (2002). Flow characteristics at drops. Journal of Hydraulic Engineering, ASCE, 128(8), 788-791.

Gaskin, S., T. Aubel and G. Holder (2003). Air demand for a ramp-offset aerator as a function of spillway slope, ramp angle and Froude number. CD-Rom Proceedings of the 30th IAHR Congress, Thessaloniki, Greece.

Gonzalez, R. C. and R. E. Woods (2008). Digital Image Processing. the 3rd edition, Prentice Hall, NJ, USA, 107-140.

Gonzalez, R. C., R. E. Woods and S. L. Eddins (2009). Digital Image Processing Using Matlab. the 2nd edition, Gatesmark Publishing, 102-106.

Jensen, A., J. K. Sveen, J. Grue, J. B. Richon and C. Gray (2003). An experimental study of wave run-up at a steep beach. Journal of Fluid Mechanics, 486, 161-188.

Johnson, R., J. Feeund and I. Miller (2011). Probability and Statistics for Engineers. Prentice Hall, Pearson Education, Inc., New York, USA.

Kiyani, G. A. and N. Rajaratnam (2008). Discussion: Experimental study on mean velocity characteristics of flow over vertical drop. Journal of Hydraulic Research, IAHR, 46(3), 424-425.

Kramer, K., W. H. Hager and H. E. Minor (2006). Development of air concentration on chute spillways. Journal of Hydraulic Engineering, ASCE, 132(9), 908-915.

Lin, C., S. C. Hsieh, K. J. Kuo and K. A. Chang (2008a). Periodic oscillation caused by a uniform flow over a vertical drop energy dissipater. Journal of Hydraulic Engineering, ASCE, 134(7), 948-960.

Lin, C., W. Y. Huang, S. C. Hsieh and Chang, K. A. (2007). Experimental study on mean velocity characteristics of flow over vertical drop. Journal of Hydraulic Research, IAHR, 45(1), 33-42.

Lin, C., W. Y. Huang, S. C. Hsieh and K. A. Chang (2008b). Reply to the discussion of: Experimental study on mean velocity characteristics of flow over vertical drop. Journal of Hydraulic Research, IAHR, 46(3), 424-428.

Liu, C. S. (2007). High-Speed Aerated Flow. China Water & Power Press, Beijing, China.

Marchi, E. (1993). On the free overfall. Journal of Hydraulic Research, IAHR, 31(6), 777-790.

Moore, W. L. (1943). Energy loss at the base of free overfall. Transactions of ASCE, 108, 1343-1360.

Pfister, M. (2011). Chute aerator: steep deflectors and cavity sub-pressure. Journal of Hydraulic Engineering, ASCE, 137(10), 1208-1215.

Rajaratnam, N. and M. R. Chamani (1995). Energy loss at drops. Journal of Hydraulic Research, IAHR, 33(3), 373-384.

Rand, W. (1955). Flow geometry at straight drop spillways. Proceedings of American Society of Civil Engineers, 81, 1-13.

Rutschmann, P. and W. H. Hager (1990). Air entrainment by spillway aerators. Journal of Hydraulic Engineering, ASCE 116(6), 765-782.

Schlichting, H. (1979). Boundary Layer Theory. McGraw-Hall, New York, USA.

Vischer, D. L. and W. H. Hager (1995). Energy Dissipators. IAHR, Hydraulic Structures Design Manual No. 9, A. A. Balkema, Rotterdam, Netherlands.

Yang, J., C. Lin, Y. D. Li, Y. H. Fu and G. W. Tseng (2014). Visualization and measurement of two-phase flow field around an aerator using PIV and BIV techniques. Digital Proceedings of the 4th Conference on Experimental Fluid Mechanics (August 12-15), BUAA, Beijing, China.

Yuan, S. W. (1967). Foundations of Fluid Mechanics. Prentice Hall, New Jersey, USA.